UNIVERSITY OF CALIFORNIA,
IRVINE

Fast Ion Transport and Losses in the DIII-D Tokamak

DISSERTATION

submitted in partial satisfaction of the requirements
for the degree of

DOCTOR OF PHILOSOPHY

in Physics

by

Kenneth Gage

Dissertation Committee:
Professor William Heidbrink, Chair
Professor Zhihong Lin
Professor Laszlo Bardoczi

2024

DEDICATION

To my nephews
Grow up and find something that fascinates you.

TABLE OF CONTENTS

LIST OF FIGURES

LIST OF TABLES

ACKNOWLEDGMENTS

I would like to thank my advisor, Prof. Bill Heidbrink, for his tutelage during my graduate career. I am especially thankful for his insistence on having a well-rounded thesis project, as it helped remind me of my love for hands-on diagnostic work. I am thankful for my committee members Profs. Zhihong Lin and Laszlo Bardoczi, who have put in the time to read and improve this work. I am also grateful to the staff at UCI, especially Jan Strudwick, who were invaluable in helping me through the administrative side of graduate school.

My time spent at DIII-D has come with a second set of mentors and collaborators who helped improve my work along the way. I would like to thank Xiaodi Du, David Pace, Mike Van Zeeland, Deyong Liu, and Cami Collins for stepping up and helping teach me when I had questions. I would also like to thank Jim Kulchar, David Ayala, Doug Taussig, Rick Lee, Matt Wolde, Will Carrig, and the DIII-D diagnostics team for helping me with the more practical side of upgrading a diagnostic. Special thanks go to Colin Chrystal, for being a consistent mentor to me throughout my final years; Kathreen Thome, for making my experiment run more successfully than I could have hoped possible; and Ron Ellis, who saved my diagnostic after it was horrifically damaged.

I would also like to thank my group members: Daniel Lin, who got me into rock climbing; Genevieve DeGrandchamp, my gym buddy and perpetual office partner; Alvin Garcia, who was always energized; Luke Stagner, my belay partner; Jeff Lestz, who always had an interesting idea to discuss; Javier Gonzalez-Martin, who was always a joy to be around; Kyle Callahan, who will always be my favorite; and Wataru Hayashi and Garrett Prechel, who joined late but still ended up being great buddies.

I am incredibly grateful for my friends at UCI and DIII-D, who have made this adventure a happy one. To Eric and Mike, my blood brothers, you have been overwhelmingly amazing to me, and I don't think I could ask for better friends. Tyler, Will, and Ryan, you helped keep me thinking positive in some of the harder parts of this journey, and I thank you from the bottom of my heart.

Lastly I would like to thank my family, who have supported my crazy journey through higher education.

This material is based upon work supported by the U.S. Department of Energy, Office of Science, Office of Fusion Energy Sciences, using the DIII-D National Fusion Facility, a DOE Office of Science user facility, under Award(s) DE-FC02-04ER54698, DE-SC0020337 and Spanish Ministry of Science and Innovation under FJC2019-041002-I.

Discussion from previously published works is presented in Chapter 3 with permission from IOP Publishing (reproduced from [16]). Work in preparation for submission is presented in Chapter 4 [17].

VITA

Kenneth Gage

EDUCATION

Doctor of Philosophy in Physics **2024**
University of California, Irvine *Irvine, CA*

Bachelor of Science in Physics & Astronomy **2017**
University of California, Irvine *Irvine, CA*

RESEARCH EXPERIENCE

Graduate Research Assistant **2018–2023**
University of California, Irvine *Irvine, California*

Undergraduate Research Assistant **2015–2017**
University of California, Irvine *Irvine, California*

TEACHING EXPERIENCE

Teaching Assistant **2017–2018**
University of California, Irvine *Irvine, California*

REFEREED JOURNAL PUBLICATIONS

Quasilinear critical gradient model for Alfven eigenmode driven energetic particle transport with intermittency **2021**
Nuclear Fusion (Coauthor)

Experimental investigation of beam-ion losses induced by magnetic perturbations using the light ion beam probe technique in the ASDEX Upgrade tokamak **2022**
Nuclear Fusion (Coauthor)

Impact of β_n and spectrum of n=1 applied fields on fast ion losses in DIII-D **2023**
Nuclear Fusion

First Fluctuation Measurements using an Imaging Neutral Particle Analyzer on DIII-D **2024**
In preparation

CONFERENCE PRESENTATIONS

Whistler Waves Driven by Runaway Electrons **2018**
APS DPP

Characterization of Intermittent Fast Ion Transport in DIII-D **2019**
IAEA Technical Meeting on Energetic Particles

Dependence of Magnetic Perturbation Induced Fast Ion Losses on Perturbation Spectrum and Plasma Response in the ASDEX Upgrade and DIII-D Tokamaks **2020**
APS DPP

Fast Ion Losses Driven by Applied Magnetic Perturbations and Plasma Response on DIII-D **2021**
APS DPP

Fast Ion Losses and Plasma Response Induced by externally Applied Magnetic Perturbations on DIII-D **2021**
IAEA Technical Meeting on Energetic Particles

Intermittent Fluctuations of Fast Ions Across Phase Space on DIII-D **2022**
APS DPP

Fluctuation Measurements of Neoclassical Tearing Mode using Imaging Neutral Particle Analyzer on DIII-D **2023**
APS DPP

ABSTRACT OF THE DISSERTATION

Fast Ion Transport and Losses in the DIII-D Tokamak

By

Kenneth Gage

Doctor of Philosophy in Physics

University of California, Irvine, 2024

Professor William Heidbrink, Chair

Fusion energy research is working toward the goal of using fusion as a source of clean energy. Since energetic particles are the main source of heating in current and future devices, understanding fast ion transport and loss mechanisms is vital. Experimental research in this thesis uses two main fast ion diagnostics, the fast ion loss detector and the imaging neutral particle analyzer, to discern how energetic particles are transported in the presence of various magnetic perturbations. First, fast ion losses in the presence of externally applied, 3D magnetic fields are analyzed. Second, transport of confined particles and simultaneous losses are observed and discussed in the presence of a neoclassical tearing mode. Lastly, work on intermittent fast ion losses in the presence of multiple Alfven Eigenmodes is observed.

Chapter 1

Introduction

1.1 Fusion Plasmas

Fusion is the process of combining nuclei into heavier elements. For very light elements, there is a significant difference in the binding energy of the reactant nuclei and the fusion products that result from the reaction (See Fig 1.1). This energy difference is released as kinetic energy in the fusion products. This energy is what powers stars throughout the universe, and humanity hopes to utilize fusion as a way to power our way of life in the future.

Fusion comes in several flavors, with each type of reaction having a slightly different probability of occurring. This probability, often described as a cross section, is dependent on the initial energies of the reactants, as this determines if the two nuclei can overcome Coulomb repulsion to fuse at all, or if they are more likely to pass by each other (See Fig 1.2). Several

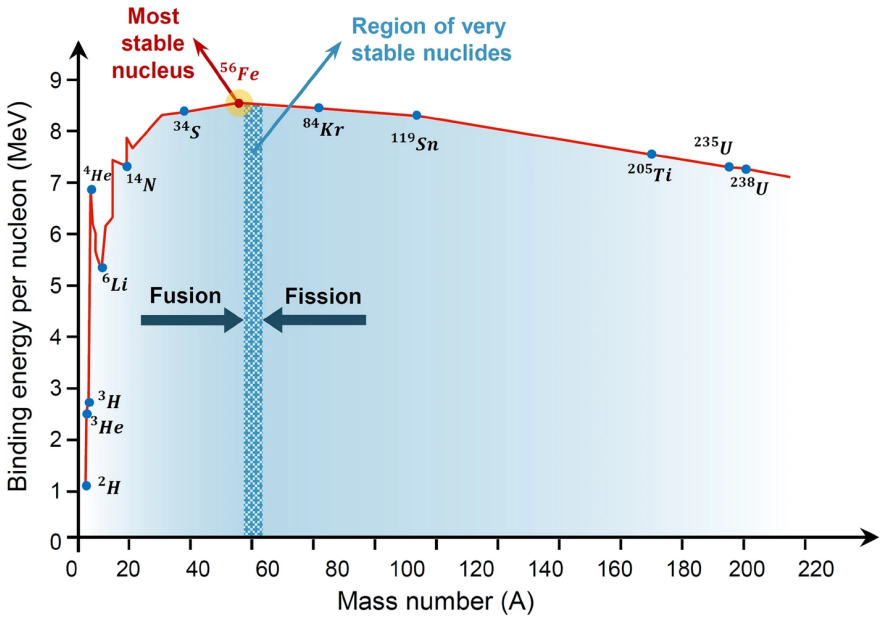

Figure 1.1: Binding energy of different element isotopes. For very light nuclei, there is a significant difference in binding energies that can be released in fusion reactions. Reproduced from [41].

common fusion reactions being discussed for research or energy purposes are as follows.

$$\mathrm{D} + \mathrm{D} \rightarrow \mathrm{T}(1.01\mathrm{MeV}) + \mathrm{p}(3.02\mathrm{MeV}) \tag{1.1}$$

$$\mathrm{D} + \mathrm{D} \rightarrow \mathrm{He}^3(0.82\mathrm{MeV}) + \mathrm{n}(2.45\mathrm{MeV}) \tag{1.2}$$

$$\mathrm{D} + \mathrm{T} \rightarrow \mathrm{He}^4(3.5\mathrm{MeV}) + \mathrm{n}(14.1\mathrm{MeV}) \tag{1.3}$$

$$\mathrm{D} + \mathrm{He}^3 \rightarrow \mathrm{He}^4(3.6\mathrm{MeV}) + \mathrm{p}(14.7\mathrm{MeV}) \tag{1.4}$$

$$\mathrm{p} + \mathrm{B}^{11} \rightarrow 3\mathrm{He}^4 + 8.7\mathrm{MeV} \tag{1.5}$$

Here the different reactants and products are mostly isotopes of hydrogen and helium. Hydrogen nuclei without any neutrons are simply protons (p), hydrogen atoms with a single neutron are referred to as deuterium (D), and hydrogen nuclei with two neutrons are called tritium (T).

For all of these reactions, the energy needed to have an appreciable reaction rate for fusion is quite high. In Fig 1.2, the energy is given in keV, orders of magnitude larger than the

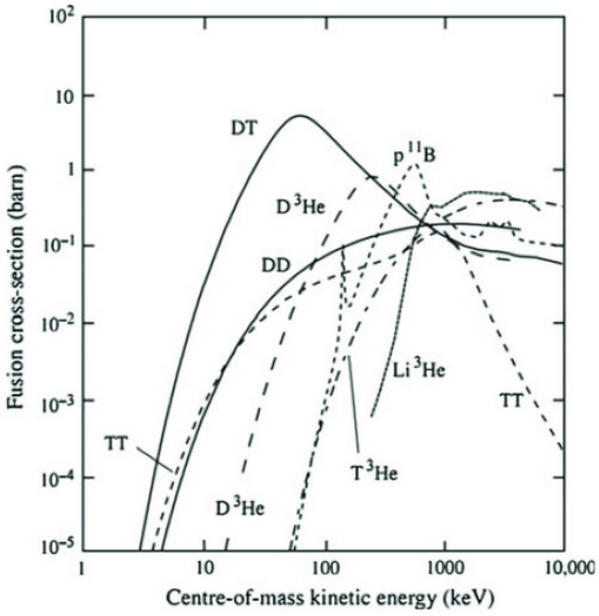

Figure 1.2: Cross section of different fusion reactions as a function of ion energy. Reproduced from [37].

energy required to strip a hydrogen nucleus of its electron. This means that fusion only happens in plasma, where ions and electrons move about separately from one another. The high temperatures of these plasmas tend to make them want to expand, so a counteracting force is required to contain them.

The most common method of containing fusion plasmas is via gravitational confinement. The enormous gravitational forces that create a star are strong enough to heat atoms to the point of ionization during gravitational collapse as well as keep the star together once fusion has begun. On earth, the problem of containing fusion plasmas is not as simple. The two most common methods are inertial and magnetic confinement. Inertial confinement is the process of using lasers or explosives to crush a fuel pellet until it fuses. Magnetic confinement, the most prevalent method in fusion energy research, uses large magnetic fields instead.

1.1.1 Tokamaks

Magnetic confinement relies on the Lorentz force,

$$\vec{F} = q\left(\vec{E} + \vec{v} \times \vec{B}\right), \tag{1.6}$$

to keep ions and electrons confined to magnetic field lines. For a simple, uniform magnetic field, charged particles are perfectly confined to field lines, and move in a helical path. For more complicated magnetic geometries, however, this is not the case. Gradients and curvature of the magnetic fields lead to drifts of the particle orbits. These drifts,

$$\vec{v}_{\nabla B} = \frac{W_\perp}{qB}\frac{\vec{B} \times \vec{\nabla} B}{B^2} \tag{1.7}$$

$$\vec{v}_R = \frac{2W_\parallel}{qB}\frac{\vec{R} \times \vec{B}}{R^2 B} \tag{1.8}$$

prevent the particles from following a single field line. Here, $W_\perp$ and $W_\parallel$ are the energy of the perpendicular and parallel components of the velocity with respect to the magnetic field, q is the particle charge, B is the magnetic field, and R is the curvature radius of the magnetic field.

One of the most common fusion devices used for research is the tokamak (See Fig 1.3), a toroidal (donut-shaped) device that keeps a plasma contained to a ring. The main toroidal field coils generate the strong toroidal magnetic field that forces electrons and ions to flow around the donut; however, this field is curved and decreases in strength at higher radii. This would lead the curvature and gradient drifts to force charged particles to move vertically out of the plasma, but the tokamak accounts for this with a poloidal field. The plasma is rotated in the machine to create a current that generated a poloidal field component. This makes the total field helical in nature, so that particles cannot escape so easily.

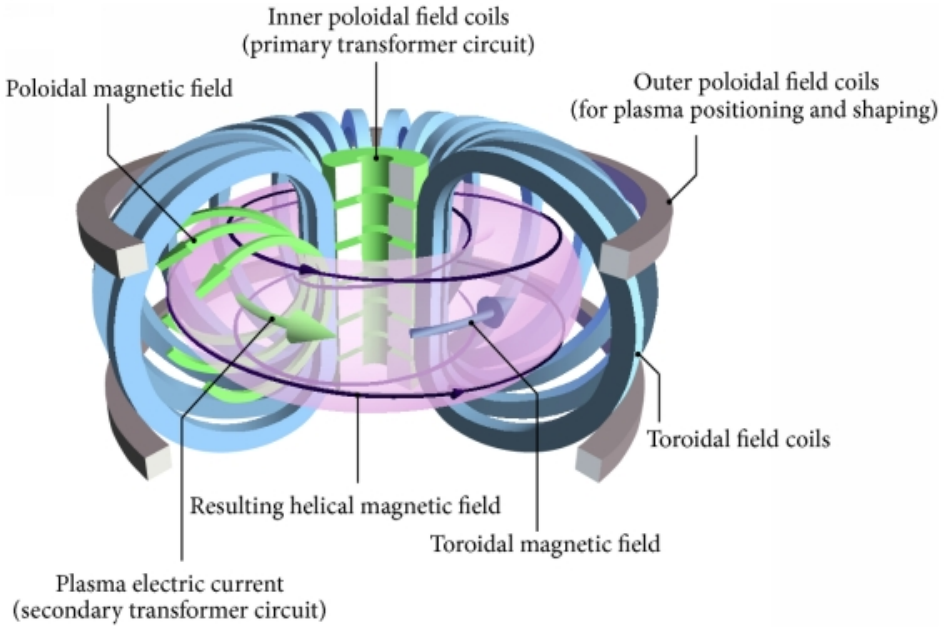

Figure 1.3: Simple illustration of the magnetic coils and fields in a tokamak. Shown in black is a single, helical field line that traverses the device. Reproduced from [34]

1.2 Energetic Particles

Heating a plasma to fusion relevant temperatures is done by creating a population of energetic particles (EPs): ions or electrons that have orders of magnitude more energy than the bulk plasma. These EPs then slow down and impart their energy into the main plasma via Coulomb collisions. In a burning plasma, the fusion products are the fast ions that keep the plasma hot; however, in current devices, auxiliary heating is required. The two most common heating sources are neutral beam injection (NBI) and electromagnetic wave injection.

Neutral beams directly insert fast ions into a plasma by injecting them as neutral particles. To generate the neutral particles, a small plasma is created in a strong accelerating electric field. This electric field can impart energies on the order of 100s of keV. These fast ions are then sent through a neutralizing chamber so they retain their energy but are no longer affected by the magnetic fields that confine the main plasma chamber. Once neutralized,

these atoms can freely enter into the plasma where they become fast ions, either by charge exchange (CX) or impact ionization.

Wave heating uses either particle resonances or wave damping to give energy to particles already in the plasma. This energy can be given to the electrons or the ions. Instead of generating a new set of particles at a specific energy, like with NBI, wave heating draws out the fast tail of the electron or ion distribution. In both cases, the resulting distribution is not only non-Maxwellian, but also anisotropic.

As fast ions are an integral part of most current and future plasma devices [21], diagnosing EP confinement is of great importance to the efficiency of heating and current drive schemes. Waves in the plasma have the ability to resonate with fast ion orbits and transfer energy to them. For these orbits, a change in energy, E, leads to a change in toroidal canonical angular momentum, P_ζ [53]:

$$\Delta P_\zeta = \frac{n}{\omega}\Delta E. \tag{1.9}$$

Here, ω is the wave frequency and n is the toroidal mode number. The change in P_ζ is related to a change in radial location of the particle orbit as $P_\zeta = mrv_\phi + qrA_\phi$. This means that interactions between fast ions and waves (especially for low frequency modes) lead to radial transport of fast ions. Plasma waves, such as magnetohydrodynamic (MHD) instabilities and Alfvén Eigenmodes (AEs) are of specific concern [26]. In worst case scenarios, EPs are not only moved out of the hot core, but they can impact the vessel inner walls. This leads not only to a decrease in heating efficiency, but can also lead to damage of plasma facing components if losses are spatially and temporally concentrated.

Fast ion transport is also related to several other perturbations in plasmas. High confinement (H-mode) plasmas in tokamaks have greatly increased power and performance, but they are also susceptible to Edge Localized Modes (ELMs), periodic expulsions of particles and energy

from the plasma. Peak heat fluxes from Type I Edge Localized Modes (ELMs) are expected to be unmanageable in devices such as SPARC [30], DEMO [61], and ITER [36]. Studies suggest that not only can ELMs cause fast ion losses, but they can also accelerate EPs before they hit the walls [47]. Research into externally applied 3D fields called resonant magnetic perturbations (RMPs) has been shown to alter ELM stability [13], but these fields cause EP losses themselves.

This thesis details studies of fast ion transport and losses on the DIII-D tokamak for several types of perturbations. In Ch 2, the two fast ion diagnostics used in this thesis, the Fast Ion Loss Detector (FILD) and Imaging Neutral Particle Analyzer (INPA), are described, and recent upgrades are mentioned. In Ch 3, fast ion losses in the presence of externally applied MPs are analyzed. In Ch 4, experimental measurements of a Neoclassical Tearing Mode using the newly upgraded INPA and simulations are discussed. In Ch 5, work in progress of analyzing observations of fast ion losses and transport with multiple active AEs is shown. In Ch 6, the findings of this thesis are summarized and future work is discussed.

Chapter 2

Fast Ion Diagnostics

Fast ion measurements can be taken in various ways. Direct measurements, like with a Fast Ion Loss Detector [15, 6], can probe the fast ion population near the edge of the plasma. The fast ion population can also be measured indirectly, via charge exchange (CX) neutrals, electromagnetic radiation, or fusion product neutrons. Fluctuation measurements of the bulk plasma and magnetics are also useful for EP diagnosis as these can detect waves that interact with fast ions.

In general, the fast ion population can be described by a distribution function in 6 dimensions — 3 spatial and 3 velocity dimensions. Since the magnetic fields in a tokamak are usually approximated as being axisymmetric, the fast ion distribution is often considered axisymmetric. This is true of ions that have started undergoing Coulomb collisions, but ions that are born via neutral beam injection (NBI) start out in a non-symmetric distribution. In velocity space, a particle's motion is often reduced to 2 dimensions, with the pitch $v_\parallel / v$ giving the motion relative to the magnetic field, and the energy giving the speed. The gyroangle of the particles helical motion is usually ignored.

Each diagnostic is sensitive to a different set of fast ion orbits. This sensitivity can be

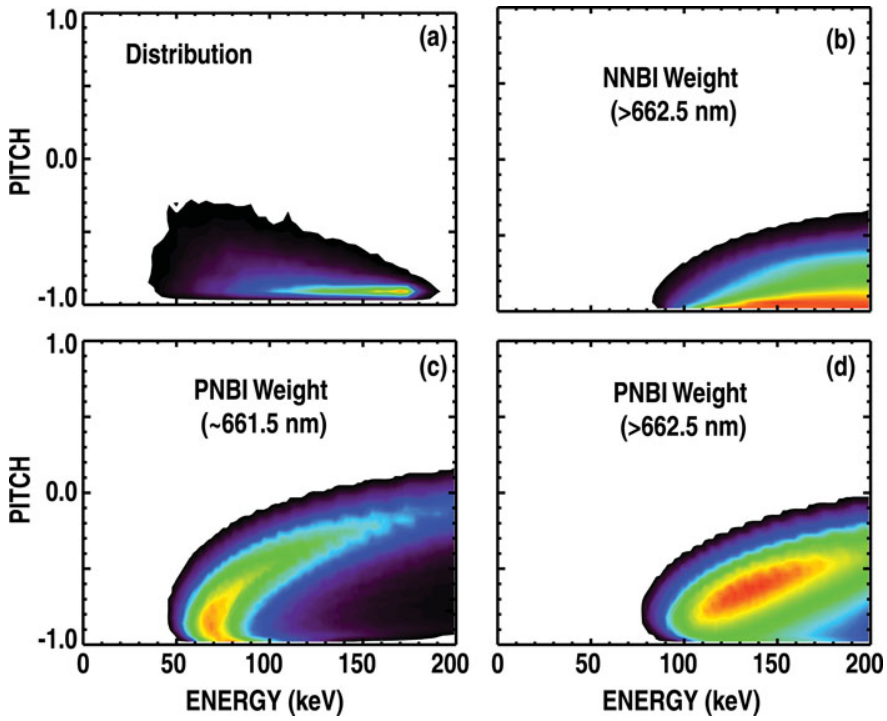

Figure 2.1: Fast ion distribution function from a neutral beam source (a) and diagnostic weight functions for different FIDA diagnostic views (b-d). Reproduced from [40].

described by a diagnostic weight function (See Fig 2.1). Often, the weight function is decided in large part due to the physical location of the diagnostic and, if applicable, its line of sight into the plasma. For example, Fast Ion D-alpha (FIDA) diagnostics measure doppler shifted Balmer alpha light from fast ions that become neutralized in CX interactions [28]. Since CX interactions require a population of neutral particles to take electrons from, FIDA signals come from localized areas along the sightline that have higher neutral densities: the neutral beam footprint, and the colder plasma edge. Fast ions in this region of physical space that can emit FIDA light that will hit the diagnoistic optics set the pitch that the measurements are sensitive to. The signals produced by the diagnostic will be based on a convolution of the weight function and fast ion distribution.

2.1 Fast Ion Loss Detectors

Fast Ion Loss Detectors (FILDs) are magnetic spectrometers that directly capture fast ions at the vessel walls. This can be done by either having the FILD built into the wall or by having a probe that can move slightly past the wall. In either case, FILDs use a small entrance aperture to ensure that ions that enter the probe will be separated by their orbits in the local magnetic field. Specifically, fast ions are separated in terms of their gyroradius (energy) and pitch. FILDs come in two variants: Faraday cups [42] and scintillator based probes [63]. Faraday cup FILDs use multiple conductive collectors to get simultaneous measurements that are sensitive to different particle orbits, while scintillator based FILDs use a combination of CCD cameras and photomultiplier tubes (PMTs) to get both high spatial and temporal resolution measurements of the fast ions that enter the probe and hit a phosphor plate (See Figs 2.2 & 2.3).

In order to determine the phase space that each section of the scintillator plate can collect ions from, a strike map is calculated based on the equilibrium fields. Extra fields, such as the ripple from the spacing of toroidal field coils can also be included, but these usually lead to minor changes in ion trajectories inside the probe head. The strike map calculation is done by initializing a set of test particles on a grid inside the diagnostic aperture and then tracing each ion until it either hits the inside of the aperture (preventing it from contributing to signal) or reaches the scintillator plate. The centroid of particle impacts is then calculated by taking the average x and y coordinates on the phosphor for each energy and pitch combination (See Fig 2.3).

This strike map can be directly overlayed on images from the CCD camera. Alignment of the strike map requires taking calibration images of the full scintillator plate. The phosphor used on the FILDs at DIII-D is TG-Green [32], which can be illuminated using UV light. Fitting the outline of the scintillator boundary used in strike map calculation on this calibration

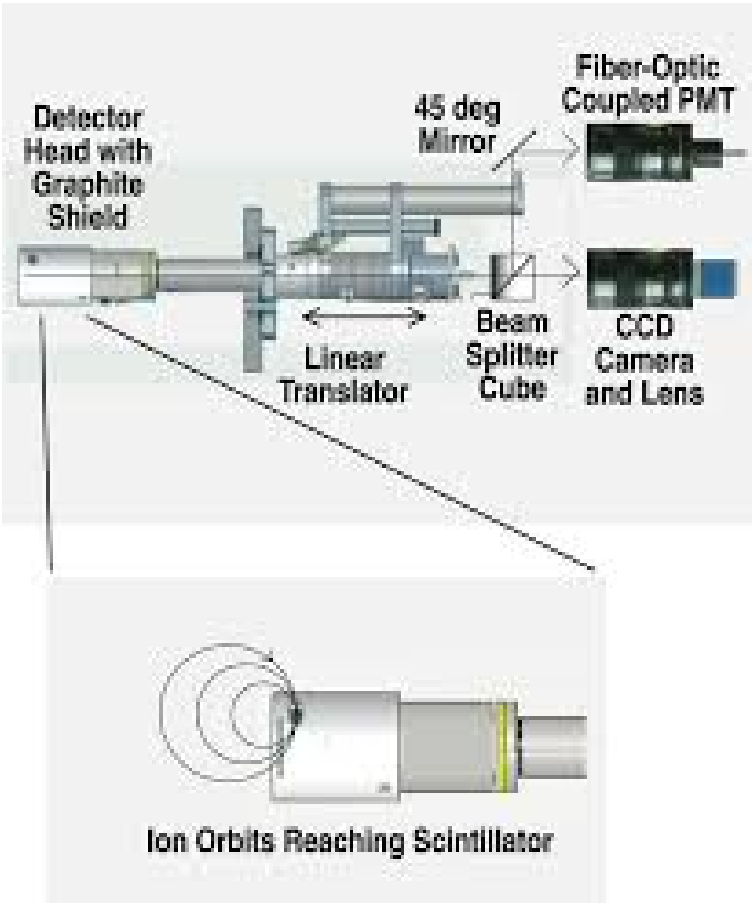

Figure 2.2: Full FILD probe diagnostic with beam optical paths to CCD and PMTs shown. Ions hitting the probe head are shown in the blown up section. Reproduced from [15].

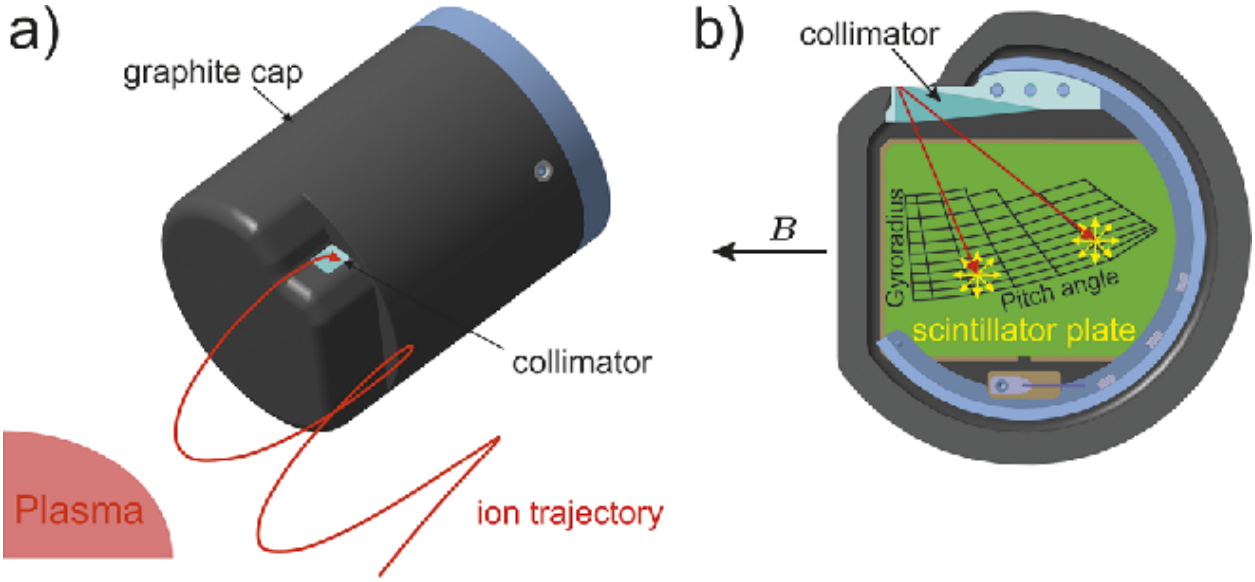

Figure 2.3: Schematic of a scintillator based fast ion loss detector. In (a), a particle orbit is seen entering the diagnostic aperture. In (b), the scintillator is shown in detail with a strike map for where each orbit will hit. Reproduced from [46].

image fixes the scaling of the strike map for experimental data. This UV illumination also works to backlight each fiber optic and determine the approximate region in phase space that each fiber is sensitive to.

While each fiber looks at a relatively large section of the phosphor compared to the size of each camera pixel, the fibers allow for measurements of losses that are coherent with waves in the plasma. The cameras on DIII-D operate at 160 fps, but the fibers are connected to PMTs that are digitized at 1 MSps, allowing for measurements up to the Nyquist frequency of 500 kHz. Since most MHD and Alfvenic activity on DIII-D has a lab frequency in the 10s or 100s of kHz, these measurements are vital to fast ion loss studies.

2.1.1 Light Ion Beam Probe

The Light Ion Beam Probe (LIBP) technique [7, 8] was developed to directly relate fluctuating loss signals to how orbits are affected by a single pass through a magnetic perturbation

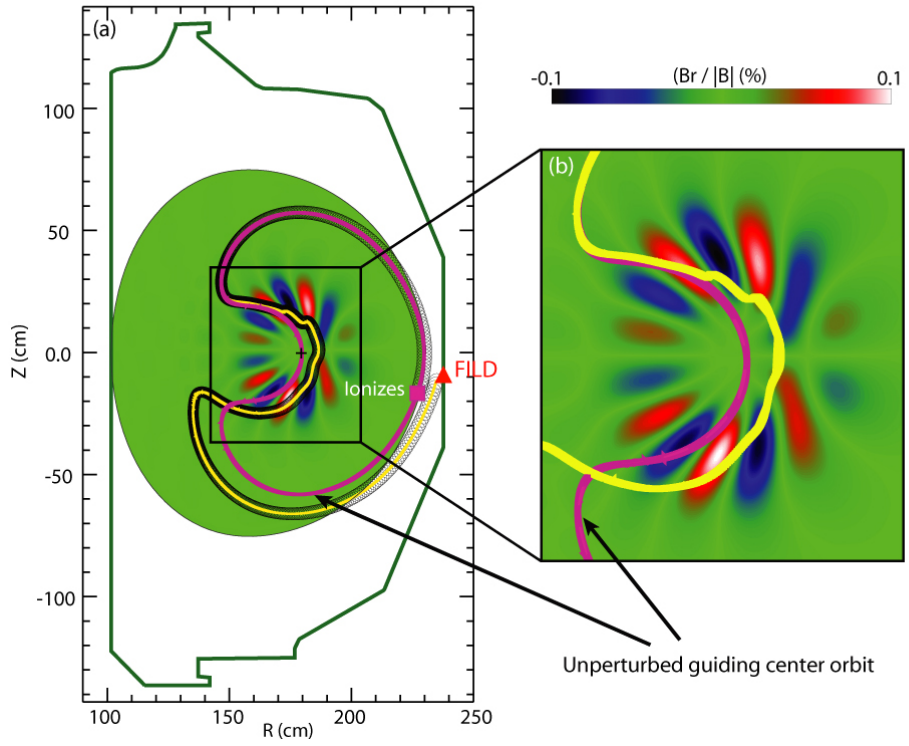

Figure 2.4: Example orbit passing through an Alfven Eigenmode and being deflected into a fast ion loss detector. The unperturbed orbit is shown in pink. Reproduced from [7].

inside the plasma (See Fig 2.4). This technique uses neutral beam ions as its test particles and specifically uses prompt loss measurements. Prompt losses refer to particles that are lost to the vessel walls on their first poloidal orbit after being ionized. This means that they only pass through the plasma — and any potential magnetic perturbations — once. Experimentally, FILD measurements that come from prompt losses can be identified by having periodic times when beam power is turned off for several milliseconds. If the losses drop out within a millisecond and restart in a similar time frame after the beam power is restored, then the signals are from first order losses.

A thorough analysis of the theory of the LIBP technique can be found in the appendix of [7], but a brief summary is included here for convenience. Fast ions from prompt losses exit the plasma on time scales that are short enough that the ions are assumed to undergo no collisions. Due to this, the phase space occupied by lost ions is conserved along their orbits,

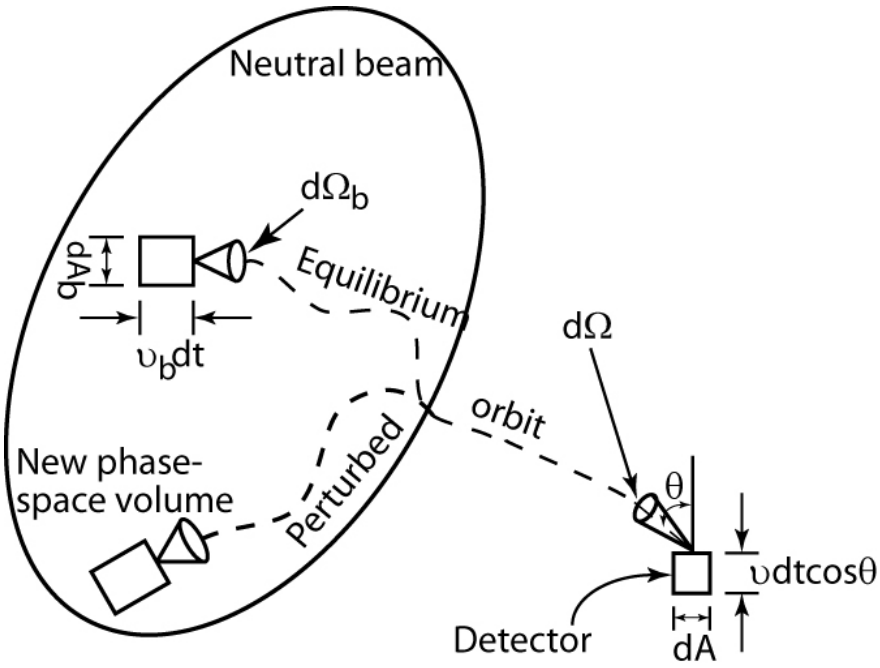

Figure 2.5: Diagram of the connection in phase space from the neutral beam footprint to the fast ion loss detector. Reproduced from [7].

and the orbits are reversible (See Fig 2.5). This means that ions can be traced back from the probe aperture to the neutral beam footprint where they were born, which is significantly easier than tracing ions from the beams forward in time to determine if they intersect the FILD.

Mathematically, the flux of ions hitting the scintillator can be calculated based on the sections of neutral beam volumes in phase space that are seen by the FILD. These volumes are weighted by the beam ionization rate at each location to reflect the number of EPs born there.

$$F = \int I \mathrm{d}A_b v_b^2 \mathrm{d}l \mathrm{d}\Omega_b \mathrm{d}v_b \tag{2.1}$$

Here, F is the scintillator flux, A_b is an area in the beam footprint emitting ions into a solid angle $\mathrm{d}\Omega$, v_b is the beam velocity, and $\mathrm{d}l$ is the differential length of the orbit as it crosses the beam. As neutral beams often have small divergence, the ionization rate can be modelled as

a spatial profile with a delta function in velocity space. Another simplification is that FILD apertures are small and usually produce well collimated signals, so the equation of the flux simplifies to

$$F_0 = \Delta A \Delta\Omega \int I \mathrm{d}l. \tag{2.2}$$

Since the LIBP technique is meant to look at perturbations, we want to determine what changes for the new orbit. We can do this by writing an orbit trajectory $\vec{\Gamma}$ in terms of an unperturbed portion $\vec{\Gamma}_0$ and a small perturbation $\vec{\zeta}$: $\vec{\Gamma} = \vec{\Gamma}_0 + \vec{\zeta}$. As long as the perturbation is small, we can expand the equation in a Taylor series:

$$\Delta F = F - F_0 \approx \int \vec{\zeta} \cdot \vec{\nabla} I \mathrm{d}A_b v_b^2 \mathrm{d}l \mathrm{d}\Omega_b \mathrm{d}v_b. \tag{2.3}$$

Here, the integral is taken over the original, unperturbed orbit. While $\vec{\zeta}$ and the gradient of I both include velocity space components, we can still take the velocity integrals to be filters for orbits that align with the beam velocity. This leaves us with

$$\Delta F / F_0 \approx \int \left(\zeta_R \frac{\partial I}{\partial R} + \zeta_\phi \frac{\partial I}{\partial \phi} + \zeta_z \frac{\partial I}{\partial z} \right) \mathrm{d}l / \int I \mathrm{d}l. \tag{2.4}$$

While this still includes all three terms of the spatial gradient, if orbits hitting the FILD are born near the center of an on-axis neutral beam, the toroidal and vertical derivatives should be negligible.

$$\zeta_R \approx \frac{\Delta F}{F_0} L_i \tag{2.5}$$

For ions born near the plasma edge, the ionization scale length L_i can be well approximated by the electron density scale length. As the DIII-D FILDs are designed to look mainly at trapped orbits, this is often the case.

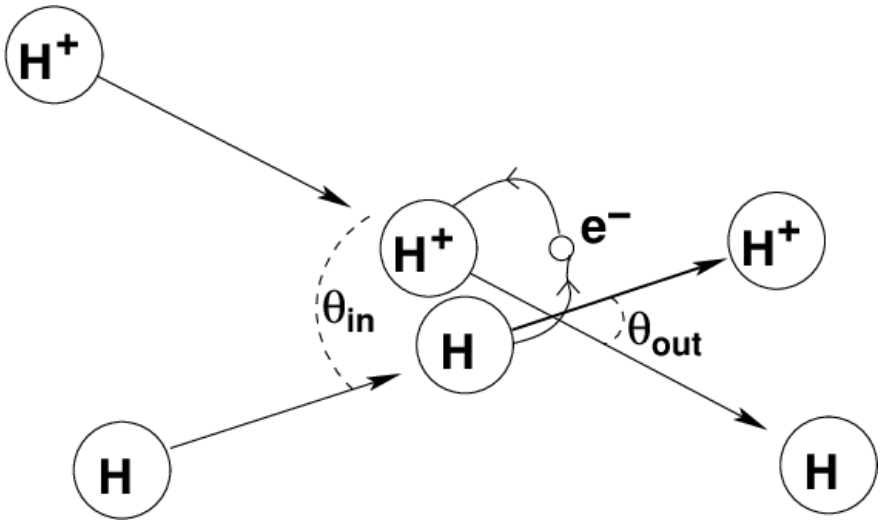

Figure 2.6: Simple representation of a charge exchange interaction. Reproduced from [25].

2.2 Imaging Neutral Particle Analyzers

Neutral particle analyzers (NPAs) take advantage of Charge Exchange (CX) interactions to diagnose confined fast ions. CX events take place when an ion and neutral particle exchange which nucleus the electron is bound to (See Fig 2.6). For EP diagnostics, this means that a fast ion that undergoes CX becomes a fast neutral and can escape the strong magnetic fields confining the plasma. NPAs take these fast neutrals and re-ionize them in order to take measurements of the fast ion population inside the plasma.

Early NPAs used an electrostatic field to separate stripped neutrals by their energy before hitting a target [1]. Later versions of the diagnostic used parallel electric and magnetic fields to separate neutral particles by both energy and charge-to-mass-ratio [22]. More recent designs included the design of solid state NPAs (SSNPAs) [62], which are more compact than previous versions of NPAs but with less energy resolution. SSNPAs were, however, able to gain more temporal resolution by operating in current mode instead of pulse counting mode.

Recently, the first scintillator-based Imaging Neutral Particle Analyzer (INPA) was designed

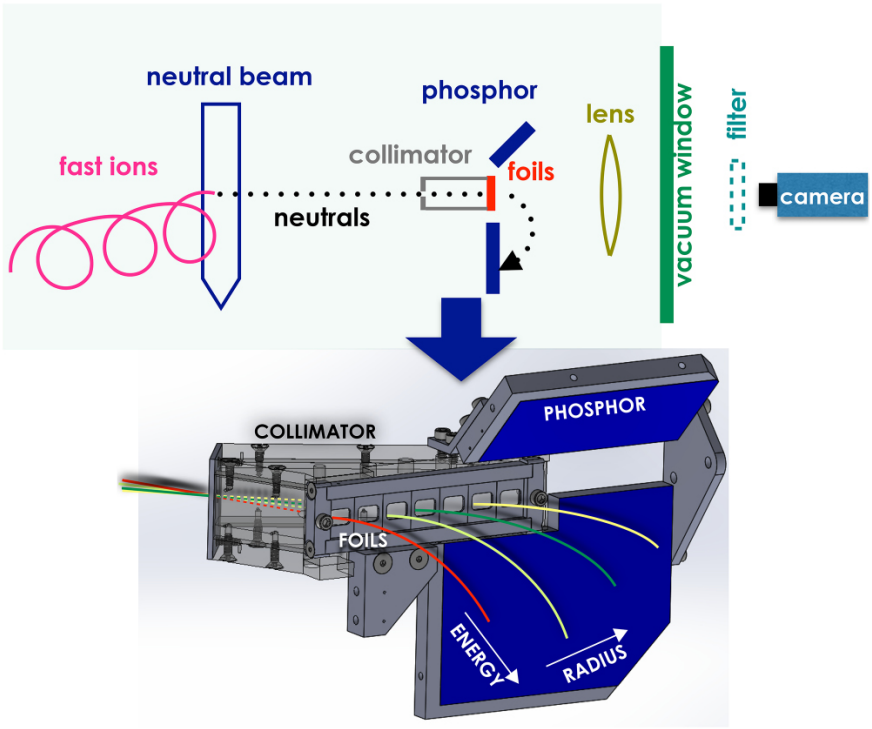

Figure 2.7: Schematic of an imaging neutral particle analyzer. Reproduced from [12].

and implemented on DIII-D. Based on the success of the scintillator-based FILD, the INPA uses the local magnetic fields of the tokamak to act as a magnetic spectrometer (see Fig 2.7). In contrast to the FILD, which splits ions by energy and pitch, the INPA discerns energy and radial location along the active neutral beam where the CX event occurred. The diagnostic neutral beam is the NBI footprint that the INPA aperture is designed to view, as a source of neutrals is required for CX interactions. The pitch of fast ions that are accepted into the diagnostic are determined by the sightline from the INPA aperture to the beam and the magnetic fields at the CX location.

While the signals in the INPA are strongest when coming from the active neutral beam in low density plasmas, cold neutrals near the vessel wall can also contribute to the signal when fast ions pass through the edge of the plasma. This signal, known as passive signal, can be modelled and separated from the expected active signal [35]. Due to the change in magnetic field between the plasma edge and core, the pitch of passive signal ions can differ

significantly from those from the active signal.

2.3 DIII-D Setup and Upgrades

The fast ion diagnostics on DIII-D include 2 FILDs and 2 INPAs — The original passing INPA, and a recently installed trapped INPA. The FILDs are displaced both poloidally and toroidally, with the first probe at a poloidal angle of 45° below the outer midplane at a machine coordinate of 225° toroidally and the second at a machine coordinate of 165° at the midplane. Both FILDs only operate when the plasma current and toroidal magnetic field are in the normal operating directions due to their aperture geometry. The INPAs are at the same poloidal location as the lower FILD probe, with the passing INPA at 285° and the trapped at 330° in machine coordinates.

The fluctuation measurements for the FILDs and INPAs were recently upgraded to allow for more FILD channels and installing new channels into the passing INPA. The FILDs now share 16 channels between the 2 probes, and the INPA has 8 fibers installed. The 1.5 mm diameter core, fused silica fibers are connected to Hammamatsu H10721-110 PMTs and Aricorp PMT 4v3 amplifiers before being digitized. The scintillating material used in the INPA was also switched to TG Green, the same phosphor used in the FILDs, when installing the fiber optics. TG Green has a response time of less than 1 μs, as do the PMTs, which allow fluctuations of up to 500 kHz to be detected without signals being complicated by response functions.

The CCD cameras for all systems were also replaced with newer, more sensitive cameras. The new pco panda cameras have higher sensitivities across the visible spectrum, a higher maximum photon count per pixel, and a larger CCD chip that can alter the region of interest (ROI) that is recorded. The ROI allows for easier alignment when reinstalling cameras, and

it allowed for us to increase the exposure time for each frame from 0.5 ms to 2.0 ms while retaining the 160 fps rate we had previously. The improved camera software also allows for the use of automatic data acquisition during experiments. This data acquisition system is explained in more detail in Appendix A.

Chapter 3

Impact of β_n and spectrum of n=1 applied fields on fast ion losses in DIII-D

This chapter discusses the effect of externally applied 3D magnetic perturbations on fast ion losses and the relationship between the plasma's response fields and orbit deflections. As the plasma response is related to β_n [44], this work looks at a set of DIII-D discharges that covered a range of β_n values to modify the plasma response amplitudes. The effect on n=1 MP induced losses over several magnetic spectra are analyzed to determine the radial displacement of lost fast ion orbits. Simulations of the discharges compare the effects of magnetic spectrum, β_n, and beam geometry on losses.

This chapter is organized as follows: In Sec 3.1, we present the setup used for the experiments on DIII-D. In Sec 3.2, we describe the results of experiments at DIII-D, most importantly the effect of β_n and the plasma response on fast ion losses. In Sec 3.3, we describe several ASCOT simulations and how the results compare with and elucidate our experimental results. Finally,

in Sec 3.4, we summarize our conclusions.

3.1 Experimental Setup

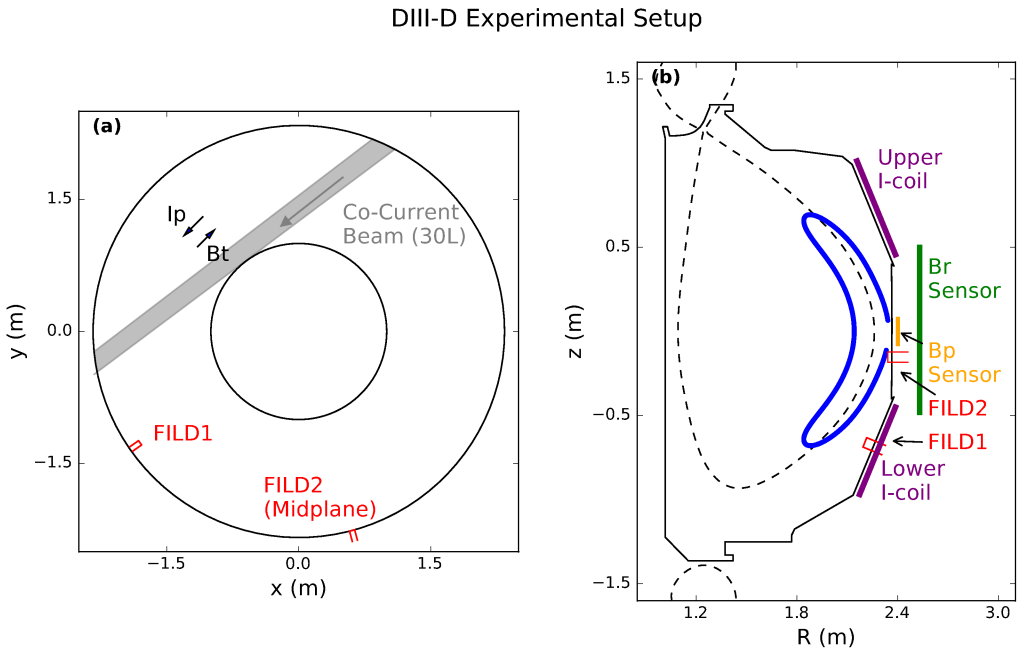

Figure 3.1: Top down (a) and poloidal cross-section (b) views of the DIII-D tokamak with experimental diagnostic locations highlighted. In (b), an example guiding center lost orbit is shown in blue.

The MPs used in this work are generated by the DIII-D internal perturbation coils (I Coils): two sets of 6 coils each, one above the midplane and one below as shown in Fig 3.1 (b). These coils can generate perturbations with toroidal mode numbers of up to n=3, but here we will focus on n=1 MPs. The I Coils are also capable of having the upper and lower sets be energized independently, allowing for a toroidal phase difference, $\Delta\phi_{UL}$, to separate the two coil sets. This $\Delta\phi_{UL}$ can be held constant while the MP is rotated, allowing diagnostics to see the full perturbation.

Measurements of the plasma response to the MPs in this work utilize the midplane magnetic probes on DIII-D [51]. Both the radial and poloidal components of the plasma response can

be measured using two separate probes as seen in Fig 3.1 (b). By selecting the component of the probe data with the frequency of the applied MP and removing the vacuum response to the I Coils, the plasma response can be obtained as discussed in [23]. Fig 3.2 shows both the full magnetic fields measured as well as the resulting calculated plasma response levels to the rotating fields. This work also uses data from the two scintillator based fast ion loss detectors (FILDs) on DIII-D [15, 6]. These are marked in both their toroidal and poloidal locations in Figure 3.1.

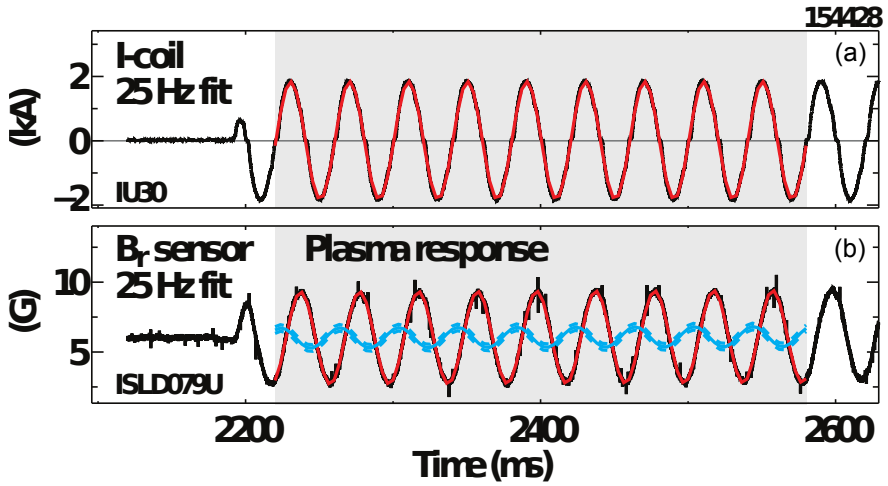

Figure 3.2: I Coil current (a) and magnetic probe data (b) during MP rotation. The plasma response after removal of the vacuum fields is shown in blue.

In order to directly relate the losses measured in the FILDs to the changes in the orbits of fast ions due to the applied MP, we use the light ion beam probe (LIBP) technique discussed in Ch 2.1.1. We ensure that the losses measured are first orbit losses by having periodic times with the beam power turned off for several milliseconds. The rotating MP then modulates the FILD signal according to the formula in Eq 2.5, reprinted here.

$$\xi = \frac{\Delta F}{\bar{F}} L_i \tag{3.1}$$

While the ionization scale length of the probing NBI source can be approximated by the electron density scale length, L_n, near the last closed flux surface (LCFS) [7], beam attenuation further inside the plasma leads to a significant change in density profiles a few centimeters

away from the edge in both L-mode and H-mode. This can be seen in Fig 3.3 (b) where the simulated beam deposition profile is compared to the measured electron density. Here, the electron temperature and density are obtained from Thompson Scattering. The beam deposition is simulated using a Monte Carlo approach using the beam geometry and plasma profiles to determine the path length of neutrals through the plasma before they ionize. Figure 3.3 (b) shows the histogram of particle markers normalized to the edge electron densities for comparison.

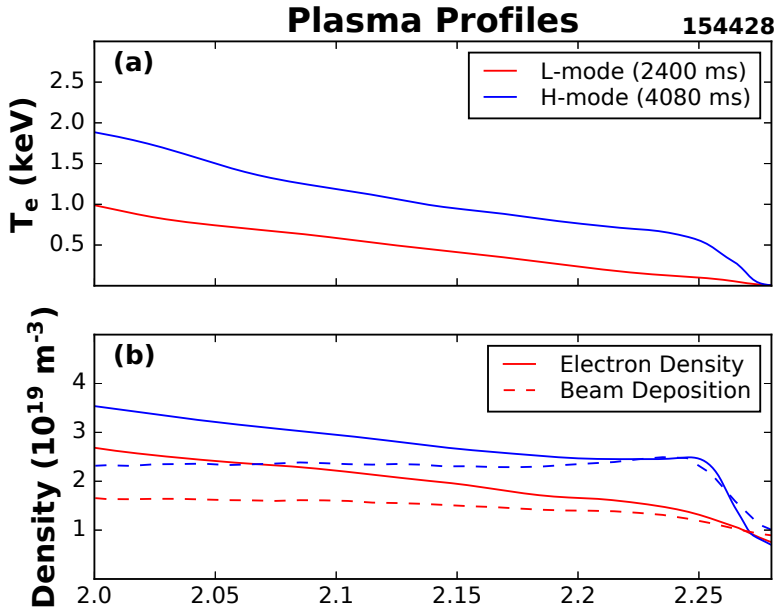

Figure 3.3: Edge temperature (a) and density (b) profiles inside the last closed flux surface. In (b), simulated beam deposition profiles (dashed) are normalized to the electron density (solid) to show the effect of beam attenuation.

The experimental data for this work is taken from a database of shots on DIII-D. A sample discharge is shown in Fig 3.4. Each shot began in L-mode and, after several MP rotation periods, was transitioned into H-mode to increase the normalized pressure β_n. The experiments ran at a toroidal magnetic field of 2 T, plasma current of 0.6–0.8 MA, and covered a range in β_n up to approximately 3.2. During the H-mode phase of these discharges, ELMs were not suppressed by the applied MPs. The n=1 MPs were generated with five toroidal phase differences, $\Delta\phi_{UL}$, of 0°, 120°, 180°, 240°, and 300°, with the 0° and 240° scenarios

being explored more in-depth. The MPs were rigidly rotated at a frquency of 25 Hz. In order to maintain a consistent injected power from the probing beam, the transition to H-mode was triggered by adding in a separate NBI source. For nearly all cases, the probing beam was a co-current, tangentially injected beam with an injection energy of 81 keV; however, a counter-current beam was used for a single 240° L-mode case for a comparison of losses due to beam geometry. The plasma current, I_p, was also lowered during the H-mode transition to maintain alignment of the NBI prompt losses hitting the FILDs. This counteracted the change in current profile caused during the transition that would otherwise alter the precession of fast ions and cause them to be toroidally displaced from the detectors.

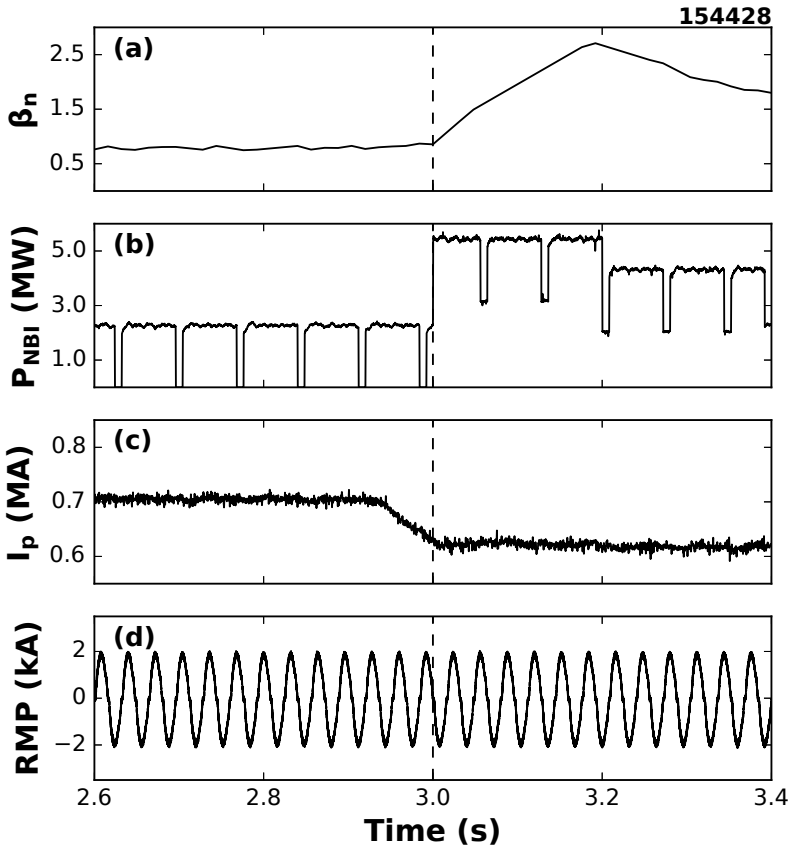

Figure 3.4: Example DIII-D shot parameters. The transition from L-mode to H-mode at 3 sec is marked with a vertical dashed line. Time traces of β_n (a), neutral beam injection power (b), plasma current (c), and current for a perturbation coil (d) are shown. The oscillation of the coil current in (d) is the 25 Hz rigid rotation of the RMP.

3.2 Experimental Results

3.2.1 Plasma Response Measurements

Measurements of the plasma response to the applied MPs allow us to translate effects of β_n on the fast ion losses via its effect on the response amplitudes. Here, we use magnetics data over one to five MP rotation periods to determine the response levels. As shown in Fig 3.5, an increase in β_n can lead to either a suppression or enhancement of the plasma response measured based on the MP spectrum. For both suppression and enhancement, the effect is most noticeable for $\beta_n > 1$ for nearly all $\Delta\phi_{UL}$. Suppression is strongest in the $\Delta\phi_{UL} = 240°$ case, but is also seen in the 180° discharges; however, the poloidal component of the response rises rapidly after $\beta_n \approx 2.4$ for the $\Delta\phi_{UL} = 240°$ MPs. Only the fully out of phase perturbations lead to suppression of the poloidal field at highest β_n. This stark difference between the radial and poloidal components may be due to a high poloidal mode number of the perturbation. Since the radial field probe is large, it averages over a larger poloidal angle, where the poloidal probe acts more like a single point detector (See Fig 3.1 (b)).

3.2.2 Fast Ion Loss Measurements

To examine the differences in losses between the two main MP spectra, $\Delta\phi_{UL} = 0°$ and 240°, we fit sinusoidal waveforms to data taken via photomultiplier tubes (PMTs) observing fast ion losses with a pitch angle of approximately 60° that impact the FILD. The PMTs are digitized at 1 MS/s, which allows for both a good estimate of the signal floor as well as the use of an ELM subtraction routine. Here we found all ELMs in a time slice that exceeded an amplitude threshold in the DIII-D filterscope data, and used this to determine an average ELM response of the PMTs. This was then subtracted off of the raw data prior to fitting a

single n=1 cosine as seen in Fig 3.6. Each time slice with a computed plasma response was fit in several 50 ms intervals, and these were combined to determine the error of the fits.

Analysis was also done using data from a camera viewing the FILD scintillator [6]. For this purpose, the section of pixels related to NBI prompt losses was integrated for each frame. There is some difficulty in determining $\Delta F/\bar{F}$ from camera data for three reasons: First, the cameras acquire images every 7 ms, leading to greater error in measurements of the background levels when the beams are off. Second, the camera exposure time is long enough that ELM bursts cannot be easily subtracted from the data as was done with the PMTs. Lastly, while the $\Delta\phi_{UL} = 0°$ discharges could often be fit to a simple sinusoidal expression, the corresponding $\Delta\phi_{UL} = 240°$ H-mode cases had more noise. Despite these issues, camera data was available for more shots than PMT data.

As seen in Fig 3.7, the PMT data points with smaller errors in $\Delta F/\bar{F}$ have values of $\Delta F/\bar{F}$ in the range of 0.2 to 0.4. There is a trend with an increase in the relative fluctuation when transitioning to H-mode for $\Delta\phi_{UL} = 240\,\mathrm{deg}$ even though the measured plasma response amplitude is suppressed. A weighted average of L-mode and H-mode time slices show a 62% increase in $\Delta F/\bar{F}$ for a 37% decrease in radial (See Fig 3.7) and 50% decrease in poloidal components of the plasma response. The larger error bars associated with the H-mode fits, however, mean that this is still consistent with the L-mode and H-mode time slices having the same relative fluctuation levels, which was also found for the camera data. PMT data for the lower FILD response to counter-current injection is similarly positioned where the nearly 50% higher relative fluctuation measurement is still consistent with being equal to the co-current NBI data.

3.3 Orbit Following Simulations

3.3.1 Simulation Setup

Simulations of four experimental time slices were run in order to better understand comparisons between cases in terms of both $\Delta\phi_{UL}$ and β_n. In order to achieve this, we choose an H-mode $\Delta\phi_{UL} = 240°$ case and a $\Delta\phi_{UL} = 0°$ slice with the same β_n value. We also choose an L-mode and H-mode time slice from the $\Delta\phi_{UL} = 240°$ shot with the best PMT data to compare the effects of β_n. A fifth simulation for the counter-current NBI case in L-mode was also run.

Magnetic fields from the MPs were simulated using a single-fluid, resistive M3D-C1 run [14]. To ensure reconstruction of the complicated effect on fast ion losses in the $\Delta\phi_{UL} = 240°$ case, we attempted to recreate the physical step function of the six physical I Coils in the upper and lower sets with the first five nonzero components in the Fourier decomposition. Results show that the plasma response to the I Coil currents is strongest at the plasma edge near the top and bottom of the plasma as seen in Fig 3.8. This pattern is seen across all simulations, with the main noticeable difference between high and low β_n being that higher β_n leads to a sharper edge.

These 3D fields were used as inputs into orbit following code ASCOT5 [58]. These simulations were initialized with markers from a beam deposition distribution, and markers were terminated after a full poloidal orbit to ensure a comparison between prompt beam losses in simulation and experiment. The importance of E_r in MP induced losses [29] led us to include the radial electric field in these simulations. The electric field was calculated using ion pressure and rotation data from the charge exchange recombination diagnostic. The H-mode discharges simulated here had E_r wells with magnitudes of 9–12 kV/m. All of these simulations were first carried out in ASCOT5 with only 2D equilibrium fields prior to in-

clusion of the MPs and plasma response in order to distinguish 2D losses from MP induced losses. The simulations used a 3D model of the DIII-D inner wall and had a 3D model of the FILD inserted at the experimental locations.

3.3.2 Simulation Results

We find that the simulations have many similarities across all co-injection NBI results. Each of the cases shows that the fast ions lost to the MPs hit the wall in midplane diagnostic ports (See Fig 3.9). Equilibrium field losses that are altered by the MPs are found in several main areas for co-current NBI: midplane ports, the lower diverter, and the inner wall at the midplane. A small number of losses were found to hit the vessel ceiling in a few H-mode simulations. Counter-current injection saw losses across the entire vessel floor up to the midplane ports. In both cases, ions that would have remained completely confined in the equilibrium fields only impact the first wall at the outer midplane once MPs are included.

The ionization locations of midplane losses are also similar for the different $\Delta\phi_{UL}$ and β_n simulations, as shown in Fig 3.10. Midplane losses originate as either trapped particles born outside the LCFS on the low-field side, or as passing particles born just inside the LCFS on the high-field side. The trapped particles hit the wall with pitches centered around $v_{\|}/v \approx 0.6$ which is consistent with the 60° pitch angle measured by the FILDs. The passing particles have a pitch close to 1, and are outside the range of pitch that the FILDs can accept experimentally [6]. Losses in counter-injection are born near the trapped-passing boundary for ions hitting the midplane and the lower FILD.

If we look at the ionization density scale lengths at the birth locations of losses in our ASCOT simulations, we find the experimental values of $\Delta F/\bar{F}$ give the radial displacement sizes in Table 3.1. In the first two rows of Table 3.1, we compare two shots with different MP poloidal spectra where we have FILD camera data. The last two rows compare the L-mode

and H-mode sections of a single plasma discharge using PMT data. In columns one and two, the phase difference between the MP coil sets and the normalized pressure show where each time slice falls in Fig 3.5. Column 3 lists the fluctuation levels measured by the midplane FILD during experiment (See Fig 3.6). The values of the density scale length in column 4 are taken at the ionization locations of ions lost in the ASCOT simulations. These two columns are input into Eq 3.1 to calculate the experimental orbit displacements in column 5. For comparison, the orbit displacements found in ASCOT simulations are listed in column 6.

The simulated results are consistent with the calculations of the experimental displacements. It should be noted that even though the experimental calculations of the orbital displacement for the ions hitting the midplane FILD shows the L-mode case to be the lowest by about 1 cm, the simulated radial displacement is higher than the simulated H-mode section of the same dischage. The experimental errors, however, mean that these results are still consistent with each other. More importantly, the displacements for H-mode plasmas are similar in both MP spectra.

DIII-D Shot	$\Delta\phi_{UL}$	β_n	$\Delta F/\bar{F}$	L_n	ξ_{expt}	ξ_{sim}
163165 (H-mode)	0°	1.9	0.31	14.4 cm	5.8 ± 1.4 cm	4.5 cm
159252 (H-mode)	240°	2.2	0.35	17.3 cm	6.0 ± 1.8 cm	4.1 cm
154428 (L-mode)	240°	0.8	0.21 ± 0.03	16.9 cm	3.5 ± 0.5 cm	4.1 cm
154428 (H-mode)	240°	1.8	0.29 ± 0.07	15.8 cm	4.6 ± 1.1 cm	3.5 cm

Table 3.1: Comparison of simulated and experimental kick sizes for co-injection losses to the midplane FILD on DIII-D.

While recent simulations on ASDEX Upgrade showed that the altered pedestal density profile due to MPs had a significant effect on the fast ion losses [18], here we have not considered any effect of the edge density perturbation. Previous work on n=2 MPs at DIII-D [57, 56] has looked into this in detail. There, simulations showed that changes due to the density fluctuations were within the noise levels of the simulations. This is because the birth locations are outside the highest density gradient of the pedestal in co-injection and well inside the

LCFS for counter-injection.

Data from the rotation of the simulated MPs shows a clear n=1 component to the midplane losses for all simulations (See Fig 3.11), including shot 159252, where the experiment showed a complicated suppression of the magnetic response. Figure 3.11 compares the ASCOT simulations of MP rotation to the experimental FILD measurements. The dependence of losses on the phase of the MPs input into the simulation agree very well with experimental measurements.

3.4 Conclusion

Here we have looked at the effects of MP spectrum and β_n on fast ion losses via the LIBP technique. This allows prompt loss measurements from a FILD to be converted into the radial displacement of lost fast ions due to a magnetic perturbation. Simulations of these plasmas can then be used to compare theory and experiment directly.

Measurements of the plasma response were taken over a wide range of β_n for several MP spectra allowing us to use β_n as a proxy for plasma response. The MP spectrum was found to have a strong effect on the relationship between plasma response and β_n, with an enhancement of the plasma response being strongest near $\Delta_{\phi UL} = 0°$, and suppression when the upper and lower applied fields were sufficiently out of phase. Suppression of the poloidal component only continues into the highest β_n for the $\Delta_{\phi UL} = 180°$ case, while the radial component remains suppressed for other MP spectra.

Even with this complicated dependence of plasma response on β_n, the birth locations of co-injected fast ion losses on DIII-D have similar birth locations regardless of β_n and the plasma response amplitude. This is consistent with EAST simulation results which suggest the plasma response's suppression of magnetic islands is counteracted by the large orbit

sizes of fast ions [24], allowing energetic particles to be lost over a wider range of response amplitudes.

The birth locations on DIII-D being in the scrape-off layer agree with work done on AUG [49], where resonant losses were found to be born just outside the separatrix, although the radial displacements on DIII-D are calculated to be a few centimeters larger. While these losses are all born outside the separatrix, the trapped orbits pass though the edge of the plasma on their inner leg, where the plasma response is strongest (see Fig 3.1 (b) and Fig 3.8). Fast ions that are transported to the edge will also be subjected to this radial kick, leading to larger delayed losses. This is not constrained to energetic particles born from neutral beam injection, but would also apply to fast ions from wave heating and fusion products.

We also show that the losses induced by n=1 MPs on DIII-D hit the vessel wall in a concentrated area in the midplane diagnostic ports. Equilibrium losses that are shifted by the MPs are also heavily concentrated here. The next largest group of shifted losses is in the lower divertor for co-injection, and on the vessel floor for counter-injection. The loss patterns here are reminiscent of results from EAST, where the MP losses have strong concentrations in the lower divertor and the outer midplane [24]. The midplane losses have the potential to be more damaging than the others as both co- and counter-current NBI led to increased losses at this poloidal location. In current and near-term devices, this area is also used for diagnostics, which can be more susceptible to damage.

Our experimental data and simulation results show that while β_n and MP spectra can have a significant effect on the plasma response, this does not always lead to a significant change in the average radial displacement of fast ions. The prompt loss nature of the fast ions looked at in this chapter also suggest the potential for further losses induced by the applied perturbation for energetic particles transported to the plasma edge. Furthermore, we find that the losses are expected to be heavily concentrated in one of the most vulnerable areas

of research devices. This suggests that diligence is required in predicting losses in future reactors, and realistic fields must be used to get accurate results.

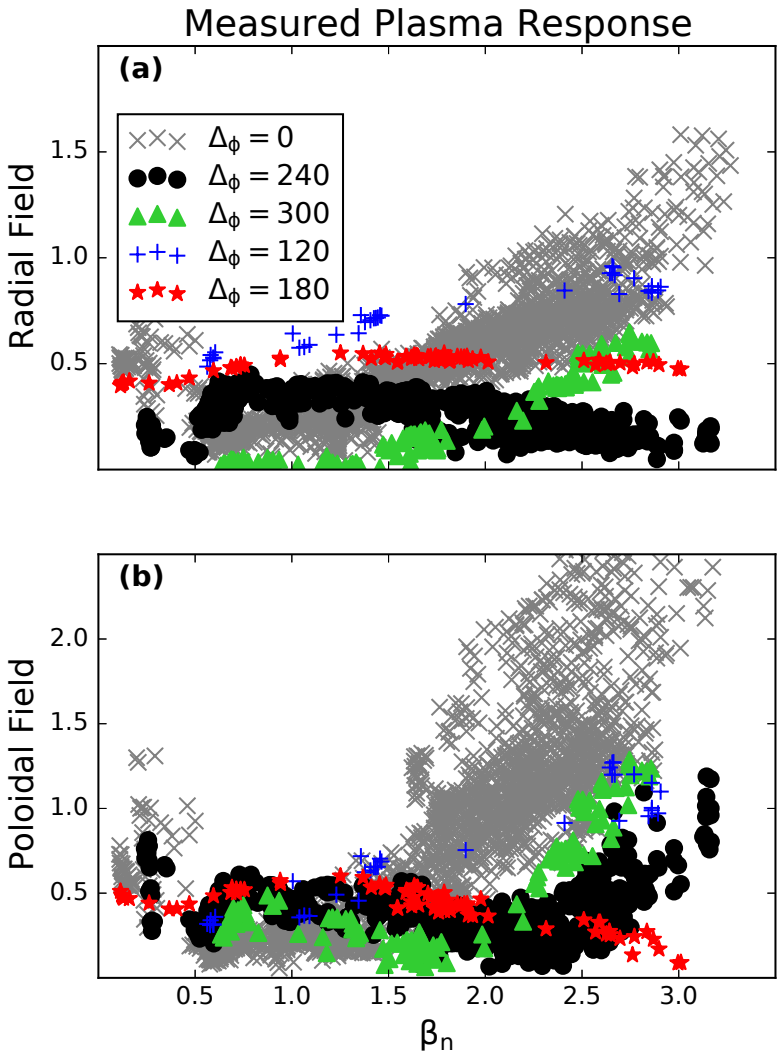

Figure 3.5: Measurements of the plasma response normalized to the I Coil current as a function of the plasma β_n for all shots in this study. On the top (a) is the midplane measurement of B_r, and on the bottom (b) is the poloidal measurement B_p.

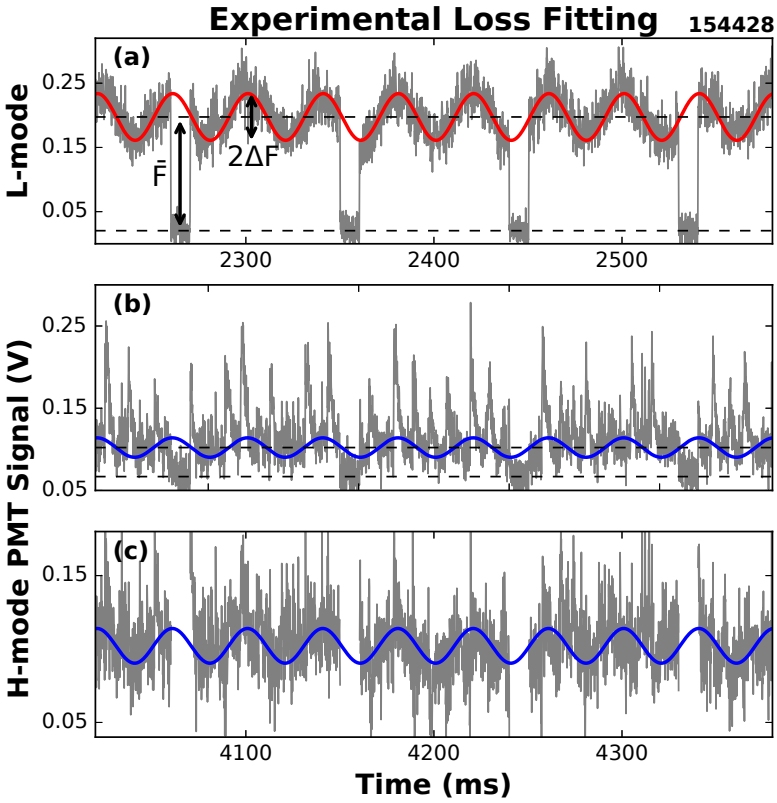

Figure 3.6: Example fits to experimental FILD data. The L-mode data (a) also shows the graphical measurements of ΔF and $\bar{F}$. H-mode data is shown before (b) and after (c) ELM subtraction. The signal is masked in (c) where the probing beam was turned off, as was done when fitting the fluctuations.

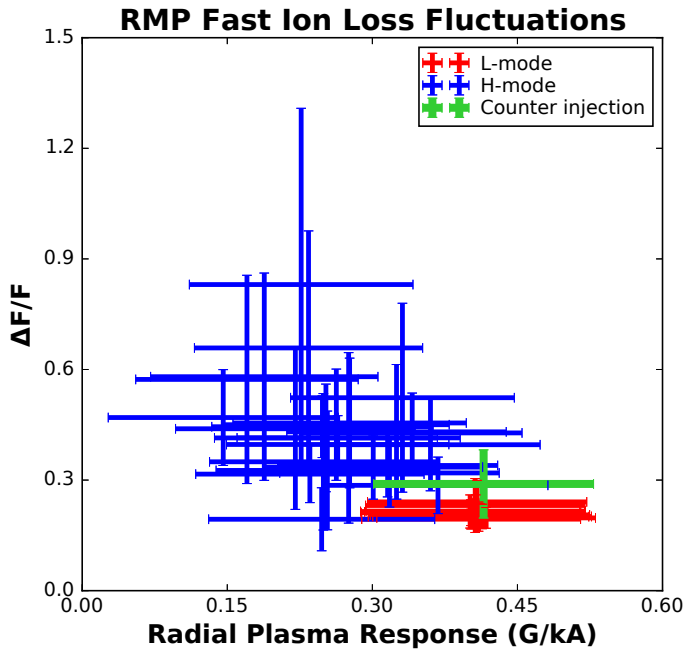

Figure 3.7: Fits of relative fluctuation levels in fast ion losses, $\Delta F/\bar{F}$, as a function of measured plasma response for $\Delta\phi_{UL} = 240\,\text{deg}$ across L-mode and H-mode.

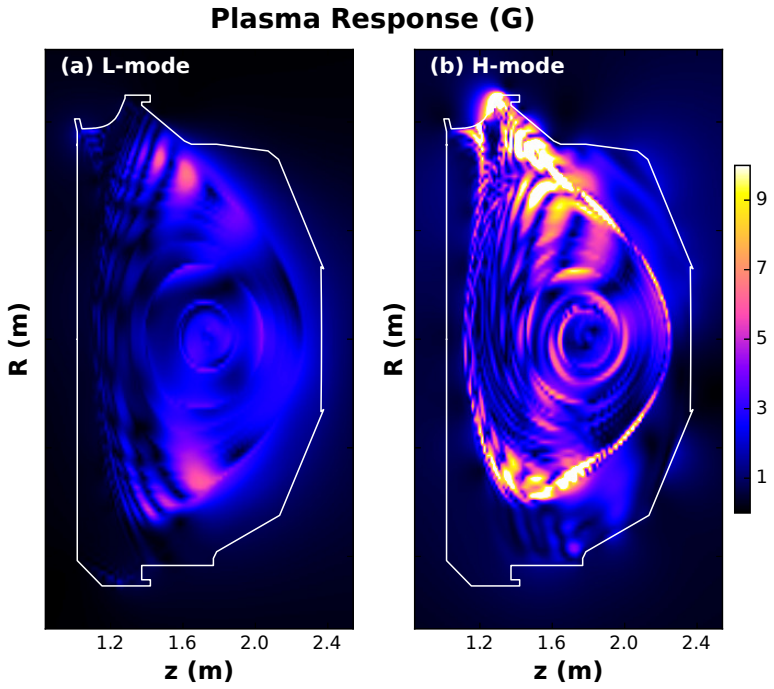

Figure 3.8: Calculated total magnitude of plasma response for (a) L-mode plasma and (b) H-mode plasma with $\Delta\phi_{UL} = 240°$.

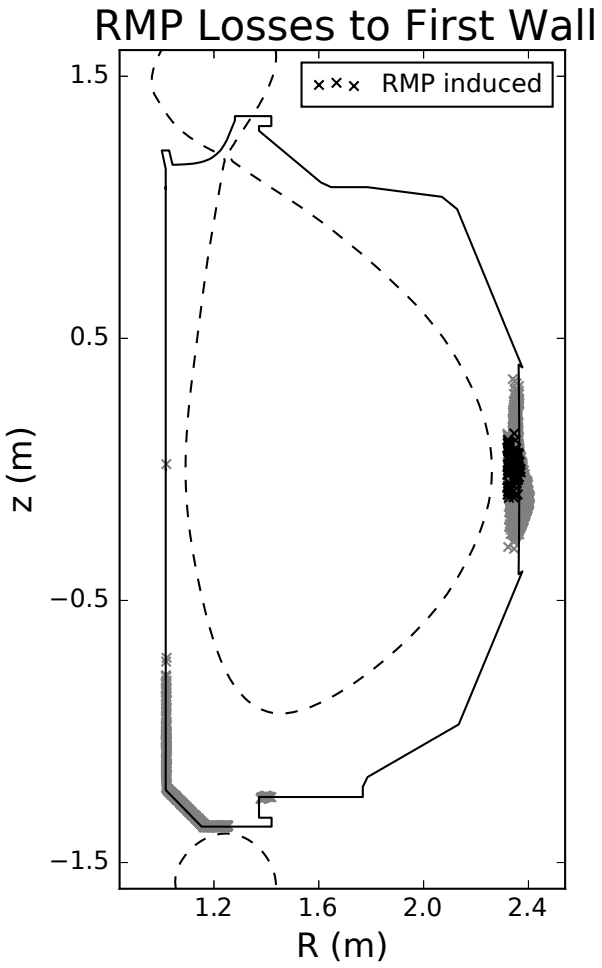

Figure 3.9: Location of neutral beam losses to DIII-D vessel walls due to inclusion of magnetic perturbations in ASCOT5 simulations. Grey markers are ions that would be lost in equilibrium fields, but the perturbations shift where they impact the vessel wall. Black markers correspond to ions that are confined in equilibrium fields, only being lost due to the applied perturbation.

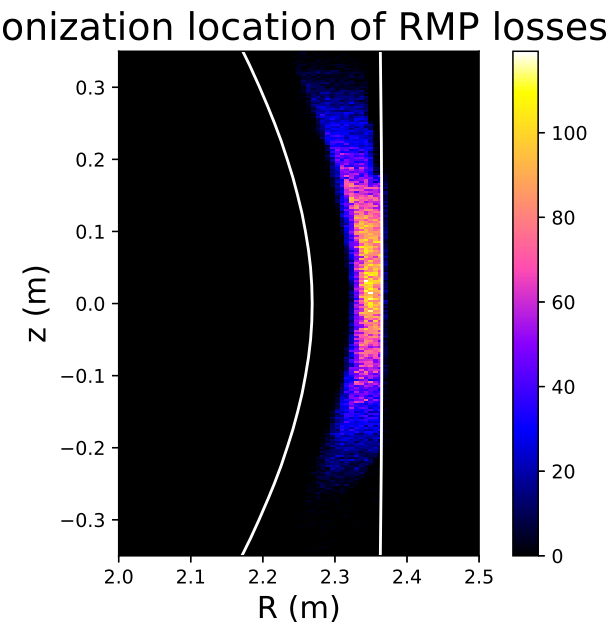

Figure 3.10: Ionization location of trapped neutral beam ions lost to the midplane port area of DIII-D in ASCOT5 simulations due to 3D magnetic perturbations. The last closed flux surface and innermost limiting surface of the outer wall are shown in white.

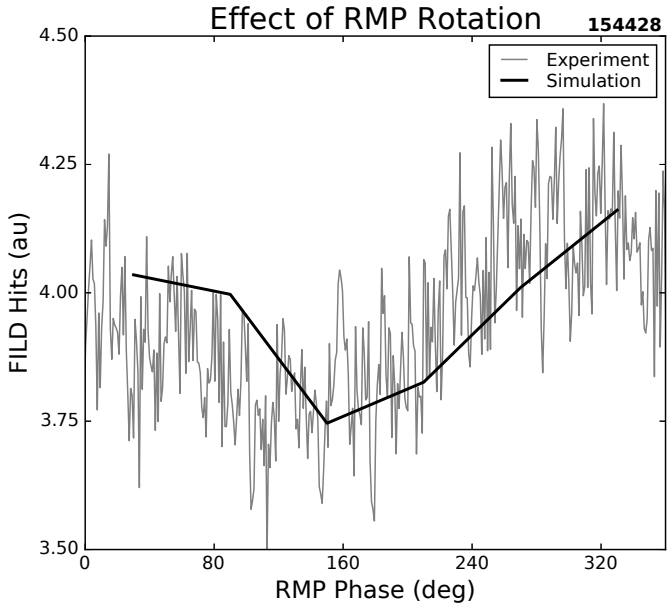

Figure 3.11: Comparison of fast ion losses to MP rotation in ASCOT for L-mode 240° case. Simulated losses are normalized to the experimental PMT signals during the time of interest.

Chapter 4

First Fluctuation Measurements using an Imaging Neutral Particle Analyzer on DIII-D

In this chapter, we present the first fluctuation measurements of a scintillator-based INPA on DIII-D from an NTM, and determine the origin of the affected fast ions. In Sec 4.1, we describe the INPA diagnostic upgrade that allowed for new measurements and the signals that can contribute to fluctuating signal. In Sec 4.2, we discuss the experimental measurements of fast ions in the plasma edge that are affected by an NTM. Sec 4.3 describes the simulations determining the origin of the measured fast ions. Finally, in Sec 4.4, we discuss our conclusions.

4.1 Diagnostic Overview

The Fast Ion Loss Detector (FILD) and Imaging Neutral Particle Analyzer (INPA) both use the local magnetic field act as magnetic spectrometers for fast ions, and separate them in based on their orbits. FILDs directly measure lost ions at the vessel wall, and the INPA ionizes neutrals that come from CX events to indirectly probe the confined population. Fluctuation measurements in this experiment were made possible due to a recent modification of the INPA to include high temporal resolution (1 MSps) measurements of the confined fast ion population. This upgrade, based on the DIII-D FILD setup (described in Ch 2.1)), uses a beam splitter to simultaneously take measurements with a CCD camera and an array of fiber optics connected to photomultiplier tubes (PMTs). Signal that passes through the beam splitter to the CCD retains the full phase space resolution of mapping the scintillator hits to their source trajectory and energy, while the fiber array acts as a grid of large pixels for observing phenomena on faster time scales. The scintillating material used in the INPA was switched to TG Green [32], the same phosphor used in the FILDs.

In general, the signal in an INPA is the flux of particles from Charge Exchange (CX) events that can be ionized in a stripping foil and measured on a scintillating plate. This flux can be related to CX with the axisymmetric slowing down distribution or with ions from a neutral beam that undergo CX on their first poloidal orbit: the latter is considered "prompt" signal. The total flux can be calculated as an integral over the diagnostic line of sight and sensitivity in phase space.

$$\Gamma = \int F_f n_0 \nu_{CX} d\vec{r} d\vec{v} \tag{4.1}$$

A fluctuating signal $\tilde{\Gamma} = \Gamma - \Gamma_0$ can arise from several sources when there is an oscillating perturbation:

1. fluctuations of the neutral population, $\tilde{n_0}$;

2. oscillations in the neutral beam ionization rate affecting the prompt signal, $F_p(\tilde{I})$;

3. advection of the slowing down population due to oscillations in the plasma equilibrium, $\tilde{F}_{sd}$; and

4. kicks from the perturbation to disturb the orbits, $F_f(\tilde{\xi})$.

While each of these terms can contribute, several are not expected to have a strong effect. Oscillating temperature and density of the bulk plasma has been shown to have an effect on prompt losses on other devices [18], but it is not expected to have a significant effect in DIII-D [57, 56]. In Sec 4.3, we will show that the neutral oscillation and slowing down terms can be ignored for this experiment, and in Sec 4.3.4 we will show that the equation for the fluctuations in INPA signal can be described using a variation of the Light Ion Beam Probe technique [7] (See Ch 2.1.1).

4.2 Experimental results

Measurements for this chapter were taken from a DIII-D discharge with a plasma current of 1.1 MA, on-axis toroidal field strength of 2.0 T, and maximum normalized pressure, β_n, of 2.4 in an upper-single-null configuration. At around 1835 ms, after beam power is increased to 7 MW and β_n hits 2.2, an NTM was driven unstable. Five neutral beam sources were used to reach this injected power level, with two beams being modulated. No electron cyclotron heating was used while the NTM was unstable. Magnetic measurements of the poloidal structure of the modes were made using the toroidal array of Mirnov coils on DIII-D [33]. Temperature fluctuations in the electron cyclotron emission (ECE) diagnostic [2] give more detail on the radial mode structure. Measurements of the lost and confined fast ion

populations were made using the Fast Ion Loss Detectors [6] and Imaging Neutral Particle Analyzer respectively.

The mode initially is measured at a frequency of 14 kHz, and over the next 150 ms, the mode locks to the vessel wall (See Fig 4.1). A set of modes with integer multiple frequencies are also detected by the magnetic coils. The Fourier decomposition code MODESPEC [52] shows the measured low frequency mode is a $m/n = 2/1$ mode, and the next lowest frequency is a 3/2 mode. Here, m and n are the poloidal and toroidal mode numbers. The third mode is an $n = 3$ mode with an m number between 3 and 5, and the fourth mode is an $n = 4$ mode. As seen in Fig 4.2, the NTM generates a set of magnetic islands that are coupled to an internal 2/1 kink mode. Mapping the ECE data to the q-profile was done using a magnetic EFIT at 1820 ms, just before the formation of the islands. This EFIT does not include Motional Stark Effect (MSE) data due to contamination from overlapping neutral beams, and this increases the uncertainty in localizing the q surfaces in the plasma. This mapping, however, shows that the NTM islands cross the calculated $q = 2$ surface at $R = 2.15$ m. This is true for all NTM frequencies detected by the ECE diagnostic, even modes where the ratio of m to n is not 2. There is also a set of islands at the edge of the plasma, around $\rho = 0.95$, that are coupled to the NTM. The lowest frequency wave is strongest at the edge, but the higher frequencies do contribute some as well.

In this discharge, three of the INPA fiber optics — designated INPA01, INPA02, and INPA07 — detected fluctuations in the confined EP population at the NTM frequency (See Table 4.1 and Fig 4.3). Since the INPA was designed to actively look at CX events with neutrals from the 330L beamline (See Fig 4.8), the ions populating this section of the scintillator are described in terms of their energy and radial location along the active beam birth profile where they underwent CX [12]. This grid of deposition locations is calculated by tracing the path of ions from the entrance of the diagnostic to the scintillator plate in the local magnetic field. The trajectories are initialized using the velocity vector of CX neutrals from the 330L

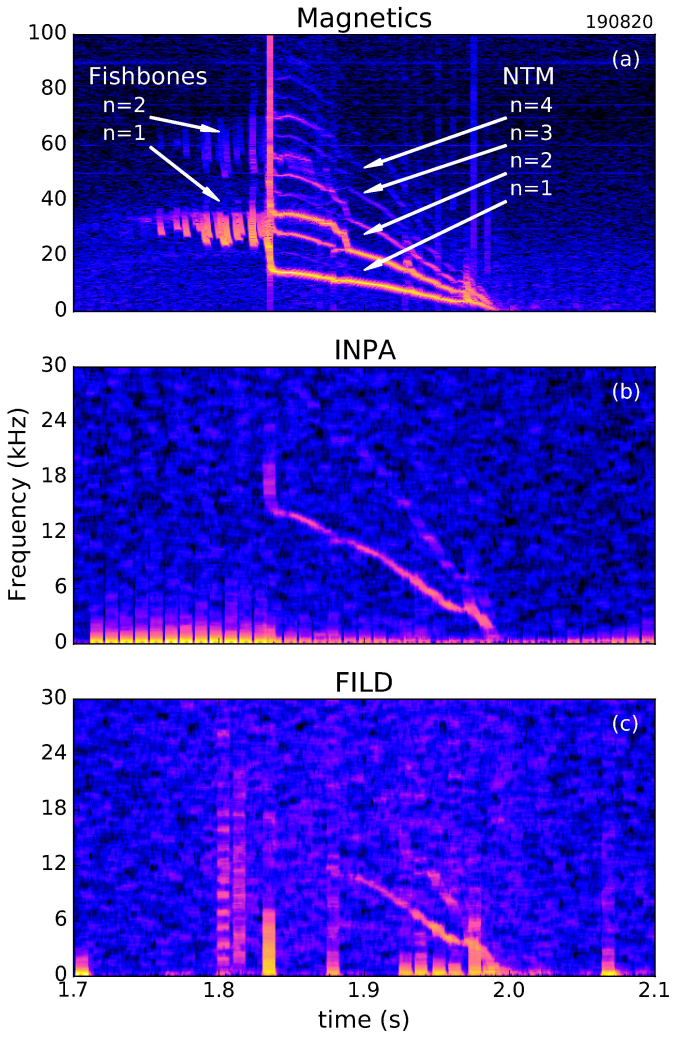

Figure 4.1: Spectra of a magnetic probe (a) and a single fiber optic view from the INPA (b) and midplane FILD (c) during an NTM. In this INPA fiber, both the lowest frequency $m/n = 2/1$ NTM mode and the next lowest frequency 3/2 mode can be seen, although the other INPA fibers only detected the 2/1 mode. Similarly, the midplane FILD detected the 3/2 mode, but the FILD at a lower poloidal position only saw the $n = 1$ mode.

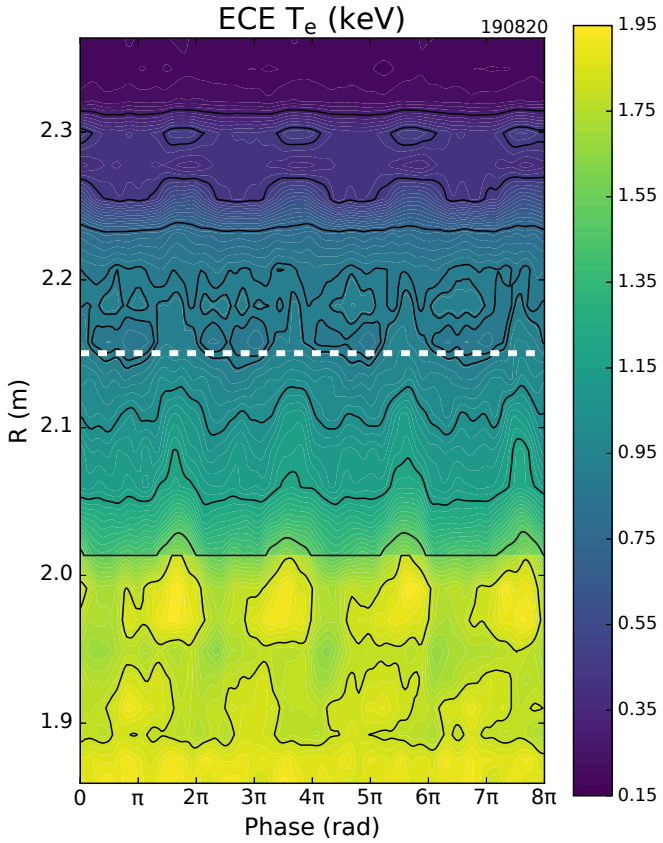

Figure 4.2: Electron Cyclotron Emission data at 1900 ms over four periods of the magnetic island structure created by the NTM (400 ms). The internal kink mode around $R = 2.1$ coupled to the tearing mode is also visible. The radius at $q = 2$ is shown in the dashed line. The magnetic axis at $R = 1.75$ m is not shown.

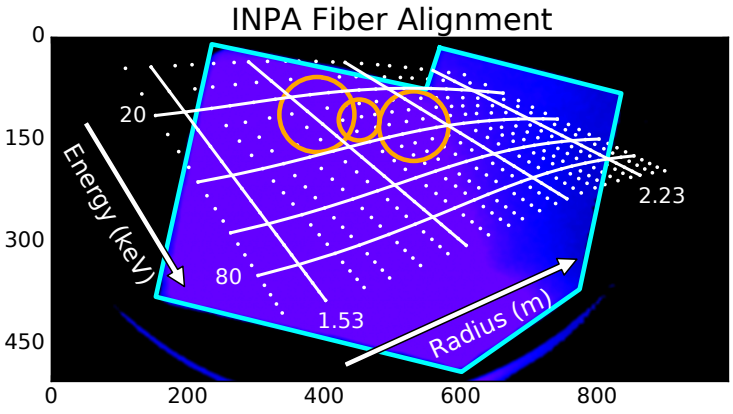

Figure 4.3: The sightlines (orange) of the three fiber optics that measured the NTM fluctuations are shown on top of the boundary of the INPA scintillator as seen by the CCD camera on the diagnostic. The fibers from left to right are INPA01, INPA02, and INPA07. Overlaid in white is a grid in Radius and Energy, showing the phase space populating the sightlines for this discharge.

Fiber	E (keV)	R_{eq} (m)	$\lvert v_\parallel / v \rvert$
INPA01	27	1.79	0.59
INPA02	30	1.87	0.63
INPA07	35	1.96	0.67

Table 4.1: The centers of each INPA fiber view in phase space. Included is the particle energy, radius along the active diagnostic beam that the view is aimed at, and pitch of particles in the plasma edge that are seen in passive signal.

beamline that intersect with the INPA aperture. These specific fibers look at low energy (20–50 keV) ions at radii in the range of 1.7 to 2.1 m. This energy range covers the third- and half-energy components of the neutral beam energies (70-75 keV) in this discharge.

PMT measurements can be broken down into 5 separate signals:

1. active signal from CX events in the diagnostic beam footprint,
2. passive signal from fast ions undergoing CX in the plasma edge with cold neutrals,
3. signal from neutron radiation entering the system,
4. 120 Hz signal from stray light, and
5. an electrical DC offset.

The last three signals must be removed in order to get good measurements of the active and passive signals. The background DC levels can be calculated from 50 ms of data taken prior to the start of the discharge, along with the amplitude of the 120 Hz signal. The neutron signal is removed by comparing data from neutron scintillators on DIII-D to INPA PMT data on shots in a reversed toroidal magnetic field. In a reverse field configuration, the helical motion of the ions moves them away from the fiber views, allowing for measurement of only the contaminating signal. This gives a linear multiplicative factor that can be used to subtract the neutron signal from the discharge. Once the INPA signal is isolated (See Fig 4.4), the signal can be compared to the diagnostic beam power to determine when

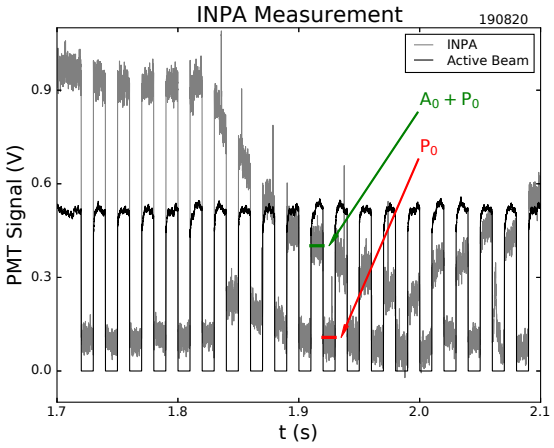

Figure 4.4: Smoothed data from the INPA07 PMT (gray) with the scaled diagnostic neutral beam power (black). The INPA data has had the background offset, stray overhead light, and neutron noise removed.

the signal is passive ($\Gamma = P_0 + \tilde{P}$), and when it is a combination of passive and active ($\Gamma = P_0 + \tilde{P} + A_0 + \tilde{A}$). The active and passive signals both change over time while the NTM is destabilized, but we can still get reasonable estimates on the time scale of the active beam modulation (10 ms).

The fluctuating amplitude can be measured by either making a spectrogram like Fig 4.1 or by using a bandpass filter at the relevant frequency range. In Fig 4.5, data from the spectrograms is shown for a 4 kHz wide band around the 2/1 NTM frequency. The fluctuation amplitude stays relatively constant for all three fibers until the frequency of the fluctuation drops out of the range used in the calculation, even though the active neutral beam was modulated; therefore, the fluctuating signal must come from passive CX in the plasma edge [35] ($\tilde{P} \gg \tilde{A}$). Reconstruction of the INPA sightlines at the plasma edge show that the range of pitches viewed by these fibers covers $0.5 \leq \left|\frac{v_\parallel}{v}\right| \leq 0.75$. The higher magnitude pitches are from the views that usually see the active beam at a higher radius. Three separate neutral beams (See Fig 4.8) were active without modulation during the NTM: the 30R (on axis, co-current, radial), 150L (on axis, co-current, parallel) and 210L beams (off-axis, counter-current, radial).

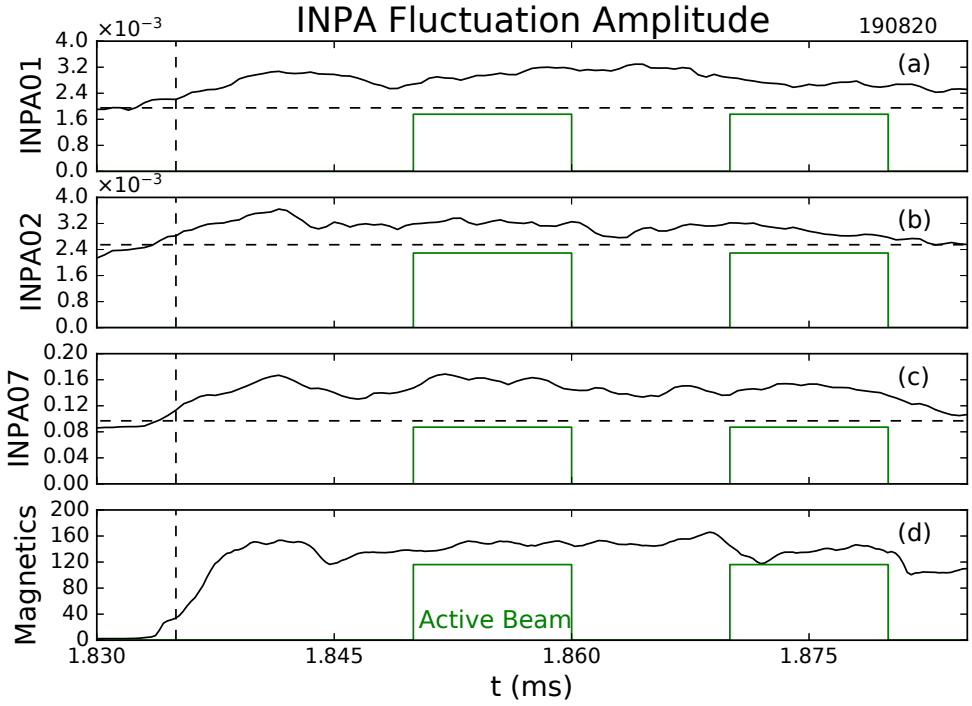

Figure 4.5: Total amplitude of fluctuations in a 4 kHz band around the NTM frequency. The INPA01 (a), INPA02 (b), and INPA07 (c) fiber amplitudes are compared to the pre-NTM amplitude (dashed horizontal). The start of the NTM is designated by the vertical dashed line. The magnetic signal strength in the same frequency band is shown in (d).

Fiber	A_0 (mV)	P_0 (mV)	$\tilde{P}$ (mV)
INPA01	3.44	2.62	1.39
INPA02	2.79	1.58	1.15
INPA07	294	108	52

Table 4.2: The measured active and passive signal levels for each fiber from 1910–1920 ms and 1920–1930 ms respectively.

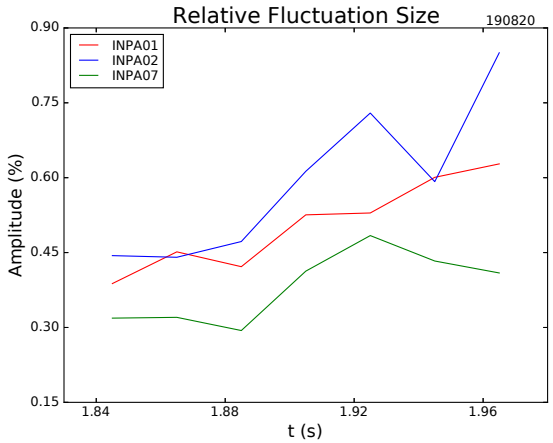

Figure 4.6: Amplitudes of the 2/1 NTM frequency fluctuations relative to the steady passive signal. The INPA02 steady passive signal level is 1.4 mV at 1965 ms.

The passive and active signals in INPA07 stay relatively constant for a short time after 1900 ms (See Fig 4.4), which allows us to get good measurements of all three components: $A_0 = 294$ mV, $P_0 = 108$ mV, and $\tilde{P} = 52$ mV (See Table 4.2 for all fibers). The fiber that sees the highest pitch views, INPA07, has a significantly higher signal strength than the other two fibers; however, the INPA07 view has the lowest amplitude fluctuation relative to the steady passive signal $\tilde{P}/P_0$. As a function of time, the relative amplitude tends to increase for all three fibers. All three fibers see the 2/1 NTM frequency fluctuations, but only the lowest pitch fiber, INPA01, is able to see the 3/2 frequency as well (See Fig 4.1(b)).

Signal from the poloidal field coil at the midplane closest to the intersection of the INPA sightline and the plasma edge shows a nearly 180° phase shift between the magnetic field near the location of the CX events and the INPA measurements (See Fig 4.7). The INPA signals show beating with multiple frequencies that are not present in the magnetics data.

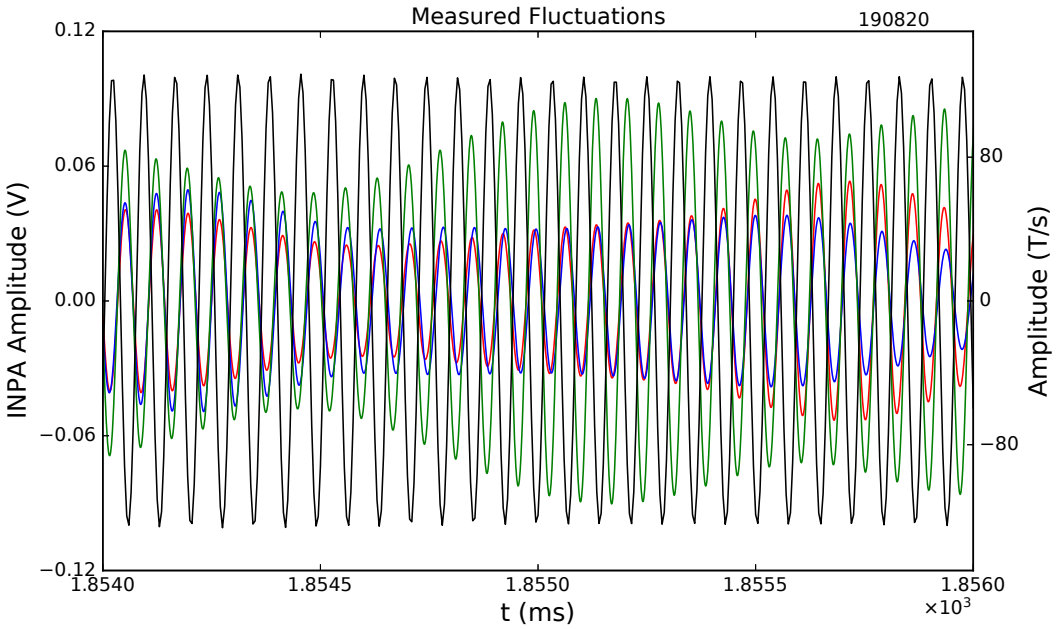

Figure 4.7: Signals from the INPA01 (red), INPA02 (blue), and INPA07 (green) fibers compared to the midplane magnetic loop at 307°(black) after filtering with a 2 kHz wide bandpass filter. The INPA01 and INPA02 signals have been scaled up by a factor of 30 for clarity. Beating of multiple frequencies can be seen in the INPA data, but the magnetic fluctuations are constant amplitude.

This is confirmed by the spectrograms, which also show signs of multiple frequency peaks. It should be noted that the amplitude of the envelopes evolve differently for each of the three fibers, suggesting that the mechanism is not identical for all phase space views.

Fast ion losses at the NTM frequency were also detected by both FILDs on DIII-D during this discharge. Losses from the 2/1 mode began hitting both detectors at approximately 1890 ms, 55 ms after the NTM became unstable. The signal then increased in strength at both detectors until the mode locked. At 1940 ms, signal from the 3/2 mode was measured by the FILD located at the outboard midplane. The detector at a lower poloidal location only saw the lowest frequency 2/1 mode. FILD fibers that saw losses at the NTM frequency were sensitive to sections of phase space corresponding to trapped particles near the full- and half-energy components of the injected neutral beams.

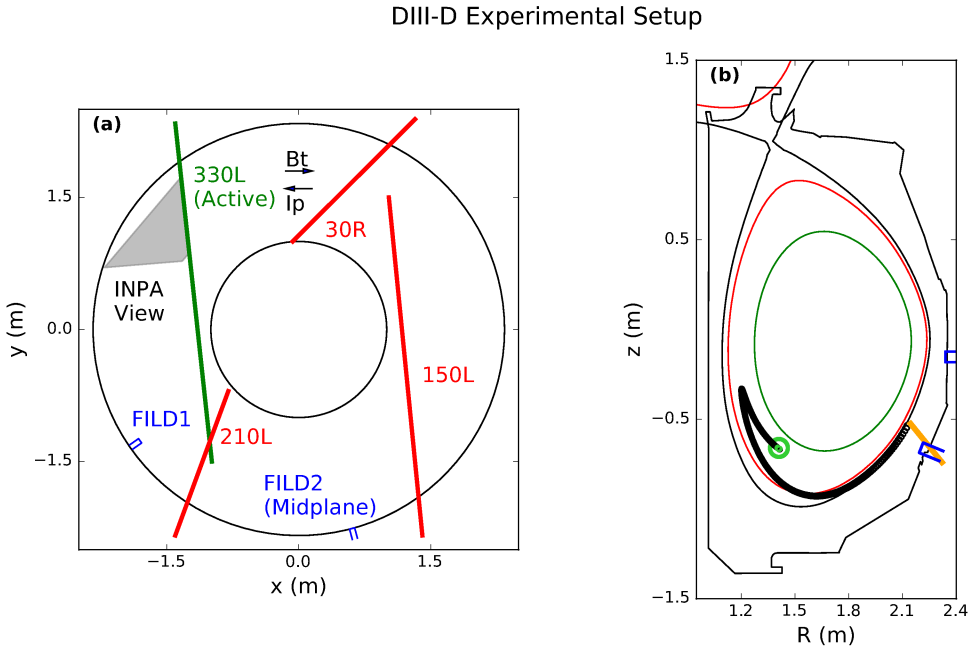

Figure 4.8: Top down (a) and poloidal cross-section (b) views of the DIII-D tokamak with experimental neutral beams and diagnostics highlighted. In (a), the INPA sightline (gray) of the active beam (green) is shown along with the beams that contribute to passive signal (red). An example orbit of prompt transport from the 210L beam is shown in (b) along with the $\rho = 0.70$ (green) and $\rho = 0.95$ (red) flux surfaces where the magnetic islands are located. The location where the orbit is born is circled, and the INPA sightline for this particle is shown in orange.

4.3 Simulated fast ion transport

In order to determine the source of fast ions to the INPA, two competing synthetic signals were calculated — one from the axisymmetric slowing down distribution, and the other from prompt, first-orbit transport of the neutral beams. Prompt transport from a perturbation affects EPs from a neutral beam source on their first poloidal orbit in the plasma, causing their orbits to shift and altering the signals of a confined ion diagnostic as they move in and out of the phase space that the diagnostic is sensitive to. For both simulations, the INPA sightline that would cross the active beam at an equivalent radius, R_{eq}, was followed until it passed through the edge of the plasma at a specific value of the normalized flux coordinate, ρ — the normalized square root of the toroidal flux. This grid spanned an equivalent radius ranging from 1.7 to 2.1 m in 5 cm intervals, and ρ was kept to the range of 0.85 to 1.1 in steps of 0.05. For a final synthetic equilibrium signal, we calculated the product of the fast ion density $n_f(R_{eq}, \rho, E)$, the edge neutral density $n_0(\rho)$, the CX cross section $\sigma_{CX}(E)$ [31], and the velocity v at each grid location. The signal was then integrated over the corresponding section of the grid that each experimental fiber was sensitive to.

4.3.1 Slowing down distribution

The slowing down distribution was calculated using the NUBEAM module in TRANSP [43]. Since the fast ion distributions from NUBEAM do not extend past $\rho = 0.95$, we had to extend these out into the scrape-off layer (SOL). This was done by noting that the fast ion density dropped sharply outside of $\rho = 0.9$, and extending that drop past the last closed flux surface (LCFS) with a fit to an exponential decay curve (See Fig 4.9(b)). This was done along 3 poloidal lines nearest the INPA sightlines. While the (R,z) locations where NUBEAM outputs the fast ion distribution in the range of $\rho = 0.85 - 0.95$ are not perfectly linear, the deviation is small compared to the expected errors in this simulation due to

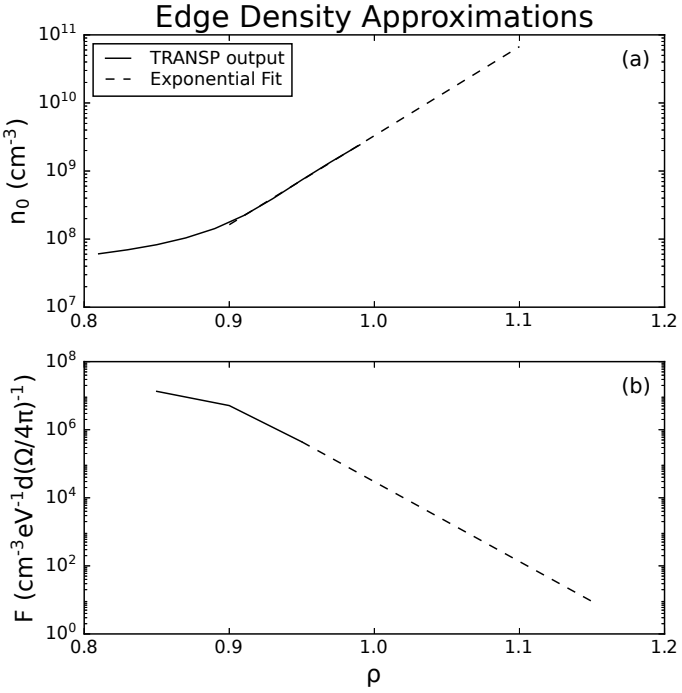

Figure 4.9: The exponential fits to the neutral density (a) and NUBEAM distribution function at pitch of 0.58 and energy of 38 keV (b) versus normalized minor radius ρ.

the use of an equilibrium EFIT. It should be noted that NUBEAM calculates the fast ion distribution based on the guiding center of particle orbits. We did not account for ion gyroradii in these calculations. Similarly, the wall neutral density output from TRANSP cut off at $\rho = 0.99$; however, this was well fit to an exponential growth curve outside $\rho = 0.9$ (See Fig 4.9(a)). The fast ion densities were then interpolated using the pitch and location of the INPA sightlines over the energy range from 10 keV to 60 keV at 5 keV intervals.

Signal from the slowing down distribution was found to be low for all three experimental INPA fiber optic views. The INPA01 fiber has the highest signal strength, but all three are of the same order of magnitude. It is also noted that the signal peaks inside the LCFS near $\rho = 0.9$ (See Fig 4.10). This is where the exponential decay of the distribution function tapers off. While the signal for the INPA01 fiber is still significant at the lowest ρ value where we calculated the synthetic signal, the strong drop off from $\rho = 0.9$ suggests that

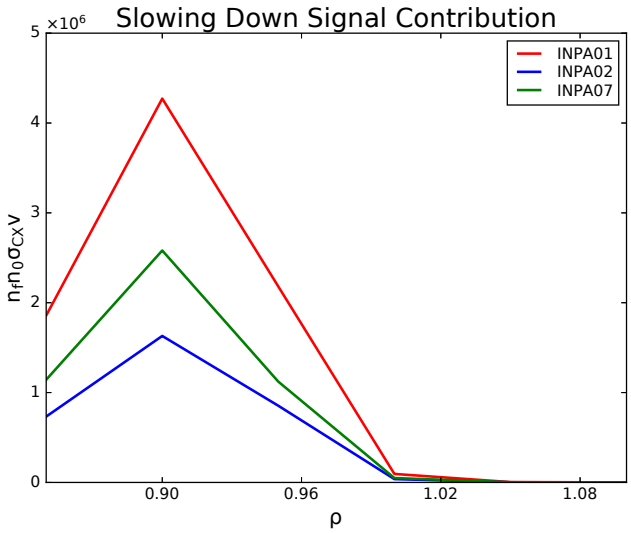

Figure 4.10: Synthetic signals for the Imaging Neutral Particle Analyzer from the slowing down distribution. Signal clearly drops off inside ρ of 0.9.

signal from further inside can be neglected.

4.3.2 Prompt transport

To determine the possibility of prompt transport contributing to the signal, the locations and pitch of the INPA sightlines were fed into a full orbit code to track the test particles backwards in time through the equilibrium fields at 1820 ms. These orbits were initialized with 6 separate energies, corresponding to the half- and third-energies of the 3 neutral beams that could have sourced the ions. The orbits were then checked to see if they passed through the birth locations for the corresponding neutral beam. This comparison was made for both the location in physical space of the beam footprint, as well as the pitch of beam ions at that location. The boundaries for the beams were made from the equilibrium and Thompson scattering density and temperature profile using a Monte Carlo code to generate millions of beam ion markers. The output of this Monte Carlo code was also used to build a 3D histogram of the beam deposition density. This was then used to sum up the contributing ions from the beams where the orbits passed through them.

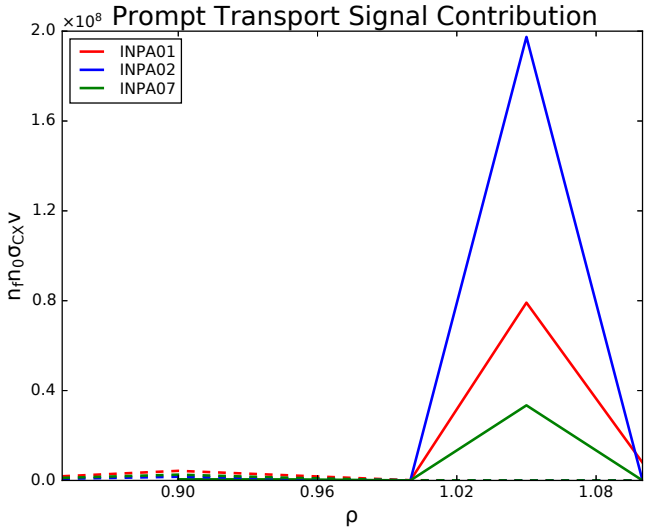

Figure 4.11: Synthetic signals for the Imaging Neutral Particle Analyzer from promptly transported beam ions are shown in solid lines. The slowing down contribution is included as dashed lines for comparison.

The prompt transport is significantly higher in amplitude than its slowing down counterpart for the synthetic signals (See Fig 4.11 and Table 4.4), suggesting that the experimental signal is almost entirely sourced from prompt transport. While the relative amplitudes of the simulated signals from prompt loss show some similarity with the relative fluctuation strengths measured in experiment, this is only the equilibrium signal that has been simulated. In these simulations, there is some error due to the course grid spacing of R_{eq} used to initialize orbits as well. Most of the synthetic signal for each fiber comes from one or two individual orbits.

The prompt signal also stands in contrast to the slowing down results in that the signal comes from just outside the LCFS at $\rho = 1.05$. This means that all of the orbits contributing to signal must pass through the outer set of islands at $\rho = 0.95$. This is the location at which the NTM interacts with most of the measured orbits. None of the orbits viewed by INPA07 pass through the NTM islands at $\rho \approx 0.7$. Similarly, the ions INPA02 is sensitive to only pass through the inner islands on deeply trapped orbits that would undergo CX at $\rho \leq 1.0$, where the neutral density is too low to generate a significant signal. The trapped orbits

Fiber	30R	150L	210L
INPA01	<1%	9%	91%
INPA02	0	1%	99%
INPA07	2%	7%	90%

Table 4.3: Relative contribution of neutral beam sources to simulated prompt signal seen in INPA fibers.

from the off-axis neutral beam that are viewed by the INPA (one shown in Fig 4.8) are born at the end of their inner banana leg, and they are only affected by the edge islands prior to CX. Only the trapped orbits at low R_{eq} are able to see the inner islands before entering the diagnostic sightline. This could explain why the INPA01 fiber is the only one to see the second-lowest-frequency signal in the experiment. Since the second-lowest-frequency was stronger in the main NTM islands at $\rho \approx 0.7$ than the edge islands, orbits that only pass through the edge would only pick up the lowest-frequency oscillations.

This is similar to the measurements with the FILD, where only the midplane probe detected oscillations at the second-lowest NTM frequency. The toroidal and poloidal displacement between the probes means that each FILD is sensitive to different orbits. This suggests that trapped orbits viewed by the lower probe do not pass close enough to the inner NTM islands to be affected by the higher frequencies, but only see the edge islands. Conversely, the midplane probe can detect orbits that traverse further inside the plasma on the inner leg of a banana orbit. This can be seen in two orbits traced back from the FILD detectors in a manner similar to what was done for the INPA (Fig 4.12).

Also of note is how each beam source contributes to the prompt signal (See Table 4.3). The 210L beam dominates in all 3 fibers, with over 90% of the signal for each. The low radial view, INPA01, only sees the third-energy orbits from the 210L; the high radial view, INPA07, is only sensitive to the half-energy orbits; and INPA02 has sensitivity to both. Similarly, trapped orbits sourced from the 150L beam at half-energy are seen by all three fibers, but only INPA01 picks up the third-energy component. The 30R beam creates signal

Fiber	Slowing ($cm^{-3}s^{-1}$)	Prompt ($cm^{-3}s^{-1}$)	Synthetic ($cm^{-3}s^{-1}$)
INPA01	8.4×10^6	8.7×10^7	9.5×10^7
INPA02	3.3×10^6	2.0×10^8	2.0×10^8
INPA07	4.9×10^6	3.4×10^7	3.9×10^7

Table 4.4: Comparison of signal strengths in each fiber for simulated equilibrium measurements. Column 1 gives the signal, $n_f n_0 \sigma_{CX} v$, from the NUBEAM axisymmetric distribution, column 2 gives the signal from the orbit following calculation of prompt transport, and column 3 gives the sum total of both simulations.

at either end of the R_{eq} grid, with deeply trapped orbits that INPA01 is sensitive to and passing orbits that are seen only by INPA07. The low levels of signal that the 30R and 150L beams contribute seems to be consistent with experiment: the measured signal from the second-lowest-frequency was weaker than the main NTM frequency in INPA01.

The particle trajectories traced back from the INPA sightlines were all on confined orbits in the equilibrium fields, but the large maximum radii of these orbits suggests that they may be close in phase space to the orbits that are lost due to the NTM. In this discharge, the FILD signals did not directly overlap in phase space with the INPA measurements, but this may be due to the toroidal displacement between the diagnostics. While we already can use an INPA and FILD simultaneously to probe both confined and lost particles, these results suggest that an INPA is also able to measure particles on loss orbits from CX events in the plasma edge.

4.3.3 Fluctuating Signal Calculations

In Sec 4.1, we described the flux of particles to an INPA in Eq 4.1 as well as the different sources of fluctuations, $\tilde{\Gamma}$, in the flux. Although 4 separate sources were listed, it is desirable to know which ones contribute significantly to experimental observations. For this work we have made simple calculations of the expected size of fluctuations that the islands in this experiment could lead to for three of the possible mechanisms.

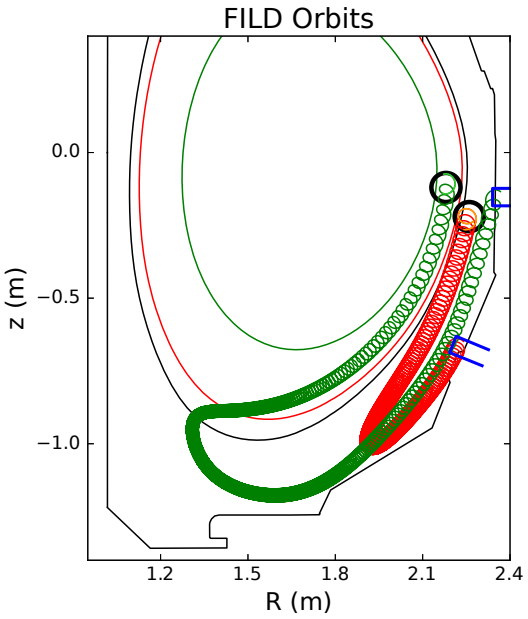

Figure 4.12: Poloidal cross-section view of the DIII-D tokamak with two orbits intersecting the Fast Ion Loss Detectors (FILDs) shown. The $\rho = 0.7$ (green) and $\rho = 0.95$ (red) surfaces where the islands are located are plotted along with the separatrix (black). The orbit intersecting the midplane FILD (green) comes within 1 cm of the $\rho = 0.7$ surface, while the orbit viewed by the lower probe (red) barely crosses inside the plasma boundary. Black circles denote the location where each ion is born.

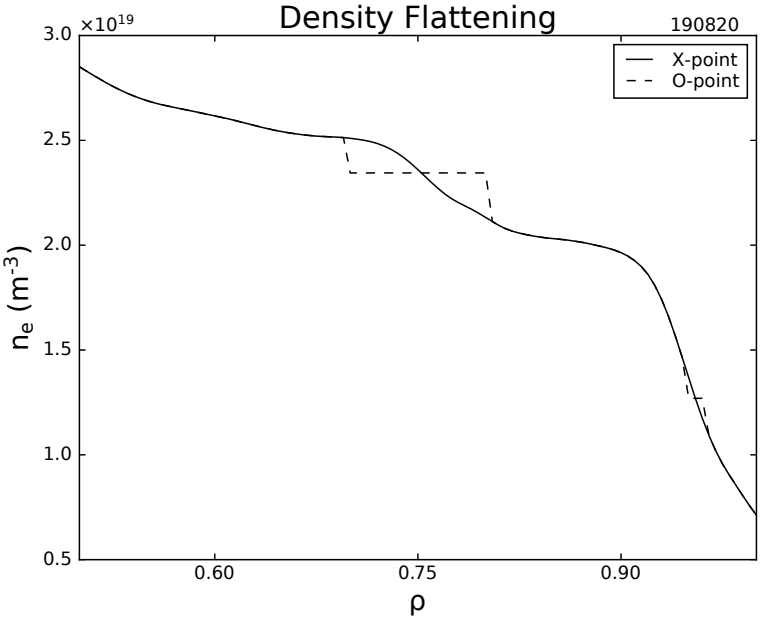

Figure 4.13: Equilibrium density profiles (solid) are plotted with a simple flattened version (dashed) that serve as a simple comparison between the X-point and O-point of the island chains.

In order to calculate the amplitude of fluctuations in the neutral density, we used the FIDASIM code [50, 20] to determine the density of halo neutrals in the plasma edge. This was accomplished by comparison of two separate density and temperature profiles to compare between. One profile was the equilibrium profile that was used to represent the X-point profile, and the other was manually flattened at the location of the NTM and edge islands (See Fig 4.13) to represent the O-point of the island chains. A low energy, 5 keV, neutral "beam" was used to initiate neutrals from the edge as a proxy for wall neutrals. The maximum deviation between the two neutral densities was on the order of 1%, below the error in the simulated results. This is also significantly lower than the fluctuation levels found in experiment.

The two profiles for the X- and O-points were also used to determine the relative fluctuations that could occur from changes in the beam ionization profile. While previous studies have seen no significant impact on edge density perturbations on fluctuating EP losses [57, 56],

Experiment	$\tilde{n}_0$	$\tilde{I}$	$\tilde{\xi} \cdot \nabla n_f$ (Slowing)	$\tilde{\xi} \cdot \nabla n_f$ (Prompt)
$\geq$30%	1%	5%	2%	<10%

Table 4.5: Relative amplitudes of fluctuations in INPA signals. The first column gives the experimentally measured values, while column 2 gives the fluctuations in neutral density, column 3 gives the fluctuations due to perturbations to the neautral beam ionization profile, and columns 4 and 5 give the fluctuations due to advection.

this was based on fast ions that were born in the plasma edge. Here, most of the prompt signal is born on the inner banana leg from the counter-injection neutral beam, between the two island chains. Generating a new set of prompt synthetic signal from the histogram of 0-point beam birth locations gave a maximum fluctuation of 4%; however, the numerical error in the histograms is 3 to 6 percent. This suggests that this may be numerical noise in the generation of beam ion markers. More importantly, this fluctuation level is also well below the experimentally measured values.

We calculated the change in the fast ion density due to advection according to

$$\tilde{n_f} = \tilde{\xi} \cdot \nabla n_f, \tag{4.2}$$

where $\tilde{\xi}$ is the distance that the perturbation moves the flux surfaces in the plasma. This distance is determined by tracking lines of constant temperature across the plasma over time in the ECE data, and ranges from 0.01 to 0.03. For the slowing down distribution, the fast ion density gradient was calculated using a second order finite difference for $\rho \leq 0.95$ and using the analytic formula for the exponential decay used for larger ρ. The prompt gradient was calculated using a first order finite difference. The maximum fluctuation for the slowing down distribution was 2%, well below the experimental value. The maximum fluctuation for the prompt signal was <10%.

4.3.4 Confined Light Ion Beam Probe

In Sec 4.3.3, we calculated the relative flux of fast ion flux to the INPA for several mechanisms. Although 4 separate sources of oscillations were listed in Sec 4.1, the effects calculated in the previous section are not large enough to account for the ¿30% relative fluctuation levels observed experimentally; therefore, we conclude that displacement of the measured orbits by the NTM ("kicks") is the dominant fluctuation mechanism. Modelling of these displacements is left for future work. Since the simulated prompt transport signal is much larger than the axisymmetric slowing down signal (See Table 4.4), kicks to the prompt orbits are considered the dominant signal. This term is

$$\tilde{\Gamma} = \int F_p(\tilde{\xi}) n_0 \nu_{CX} d\vec{r} d\vec{v}. \tag{4.3}$$

In our simulation results, we can see that the competing densities of the fast ions and neutrals create a very thin layer where CX events occur at a high rate. Assuming n_0 is a function of only ρ near the diagnostic sightline, we can use the average neutral density at the CX layer and pull it out of the integral. Since the prompt transport can only be composed of ions at the full-, half-, or third-energy components of the neutral beam, this makes the CX rate a constant for each component. This leaves only the prompt distribution function in the integrand, and conservation of phase space allows us to integrate at the appropriate section of the neutral beam birth profile instead of in the INPA sightline. A Taylor series expansion of the total flux (See Appendix of [7]) gives

$$\tilde{\Gamma} = \Gamma - \Gamma_0 \approx n_0 \nu_{CX} \int \vec{\xi} \cdot \vec{\nabla} I d\vec{r}, \tag{4.4}$$

where Γ_0 is the average flux, $\vec{\xi}$ is the orbital displacement due to the kick, and I is the ionization rate of the neutral beam. For signal from the center of an on-axis neutral beam — such as with the higher frequency signal in INPA01 here — this formula can be further

reduced.

$$\frac{\tilde{\Gamma}}{\Gamma_0} \approx \xi_r \frac{\partial I/\partial R}{I} \tag{4.5}$$

For this experiment, the neutral beams that sourced the INPA fluctuating signals were on constantly, and the steady signal from each beam cannot be properly determined; however, this method of measuring the strength of a perturbation's effect on the confined population via INPA signals can become a powerful tool in future experiments.

4.3.5 Sensitivity study

In order to see how much effect the equilibrium reconstruction had on the results, we compared an automatically generated EFIT against a custom built equilibrium. Both equilibria were tested in every stage of the process for finding the equilibrium signals, from determining the (R,ϕ,z) locations where the INPA sightlines cross the plasma edge, to the TRANSP run and orbit following procedure. The INPA02 and INPA07 signals were not strongly affected, with changes of less than 10% between the two magnetic reconstructions. The INPA01 results saw stronger amplitude changes, with the slowing down signal nearly doubling for the custom EFIT. It is possible that this sensitivity is related to the location of the trapped-passing boundary in phase space in relation to the INPA01 fiber view for the slowing down distribution. Orbits traced back from the INPA sightline near $\rho = 0.95$ showed a trapped passing boundary in this region of phase space. The prompt loss change is likely do to sensitivity of this fiber to the coarse grid spacing.

4.4 Conclusion

In summary, we have made the first fluctuation measurements of an MHD instability using a scintillator-based INPA on DIII-D. The orbits probed are on confined orbits that pass through the plasma edge and undergo charge exchange in the diagnostic sightline. The significant extent of the orbits into the SOL suggest that the INPA passive signal may be able to overlap with lost ion orbits for some magnetic geometries. Here, simulations suggest the measured fast ions were sourced from multiple beam populations via prompt transport, with a potential for some contribution from the slowing down distribution.

Calculations of the fluctuating signals suggest any mechanism other than direct kicks to the fast ion orbits cannot contribute enough to reproduce the large relative amplitudes seen in experiment. This agrees well with experimental observations of frequency beating in the INPA data. Since the NTM amplitude varies little, advection, fluctuations in the neutral density, and oscillations in the beam ionization rate are not expected to give rise to frequency splitting in INPA data, while kicks in multiple positions of the loss orbit readily produce additional frequencies in a prompt loss signal [9]. Furthermore, the difference between the evolution of the envelope amplitudes for each fiber suggests that the mechanism responsible for the fluctuations is phase space dependent.

The prompt nature of this transport suggests that with the use of proper beam modulation, the Light Ion Beam Probe technique [7, 8] may be applied to INPA passive data. This would allow for measurements of the transport caused by a magnetic fluctuation on a confined particle close to a loss orbit, which would greatly complement similar measurements using a FILD.

Our simulations indicate the measurement of the 3/2 mode is only seen by the low pitch fiber view due to sensitivity to deeply trapped orbits seen near $R_{eq} \approx 1.7$m. The particles seen in the INPA02 and INPA07 fibers are only affected by the islands at the edge of the plasma,

and particles seen by INPA01 from the 30R and 150L neutral beams likely get the higher frequency kicks from the $q = 2$ surface islands on the inner leg of their orbit. Similarly, the difference in orbits viewed by the FILDs (See Fig 4.12) explains why the 3/2 frequency was only measured in the midplane probe.

Fluctuation measurements using NPAs and other diagnostics [19], help improve our understanding of coherent EP transport. Combined with the robust resolution in energy and physical space from the dual measurement design of the INPA, the upgrades to this scintillator based design increase our ability to accurately probe the affect of magnetic perturbations on the confined population of fast ions. Given the importance of reducing EP losses and transport from the core in burning plasma devices from NTMs and other MHD and Alfvén instabilities [21, 26], these new diagnostic breakthroughs are of great benefit to future EP research. We have already begun work on improving our design to better capture fluctuations from other instabilities such as Alfvén Eigenmodes.

Chapter 5

Intermittent Fast Ion Losses on DIII-D

This chapter discusses intermittent fast ion losses in the presence of multiple Alfvén Eigenmodes (AEs). This chapter is organized as follows: In Sec 5.1, we describe some of the theory of intermittency in relation to EP transport. In Sec 5.2, we describe experimental measurements taken at DIII-D that show intermittent behavior. In Sec 5.3, we describe the intermittent signals qualitatively, and discuss contamination to the data. Finally, in Sec 5.4, we summarize our conclusions.

5.1 Background

Self Organized Criticality (SOC) is a description of systems that are slowly driven near a local stability threshold [48]. These local thresholds lead to intermittent transport when they are exceeded. Often, a sand pile is used to describe how this works: If sand is slowly poured onto a pile, the pile will build up until the gradient along the sides becomes too

much to hold up against gravity. Once this threshold is reached, an avalanche of sand will redistribute the grains until the sides are just below the critical gradient again. Intermittent behavior can be described as relating to a probability distribution with widely distributed patches of high density.

For a simple toy model (See Fig 5.1), a distribution function can be compared to a Gaussian model of random noise. A Gaussian distribution has most of its probability well localized, but a distribution like the Cauchy distribution has a "fat tail" that allows for significant portions of the probability density to be far from the average. This leads to noting that distributions that exhibit intermittent behavior can be detected by measuring high order moments of the distribution which are sensitive to avalanche-like events [38]. Another way to measure intermittency is via the Hurst parameter, a description of correlations between time steps [39, 48].

Evidence of SOC has previously been found in plasma turbulence on several devices [4, 5, 3, 45, 60]. Studies on DIII-D also show evidence of critical gradient behavior in the fast ion profile [11, 10, 27]. Data from neutron scintillators and neutral particle analyzers show a clear threshold in injected power for an increase in modulated flux in L-mode plasmas. Fast Ion D-alpha (FIDA) data also shows stiffness in the fast ion profiles as the beam power is stepped up. Each diagnostic is sensitive to a different portion of phase space, and sees a different threshold for the onset of intermittency. This chapter will be more focused on increasing losses during beam power scans.

Theory for EP losses due to critical gradient behavior is not settled, but there are a couple of candidates for mechanisms driving this transport. First, simulations using the MEGA code [54] show that in the presence of multiple toroidicity induced AEs (TAEs), overlapping of resonances can lead to intermittent transport across flux surfaces as avalanches of particles move radially across the plasma [55]. A second theory suggests that microturbulence alters the damping rate of AEs and leads to nonlinear behavior in AE transport [59]. In order to

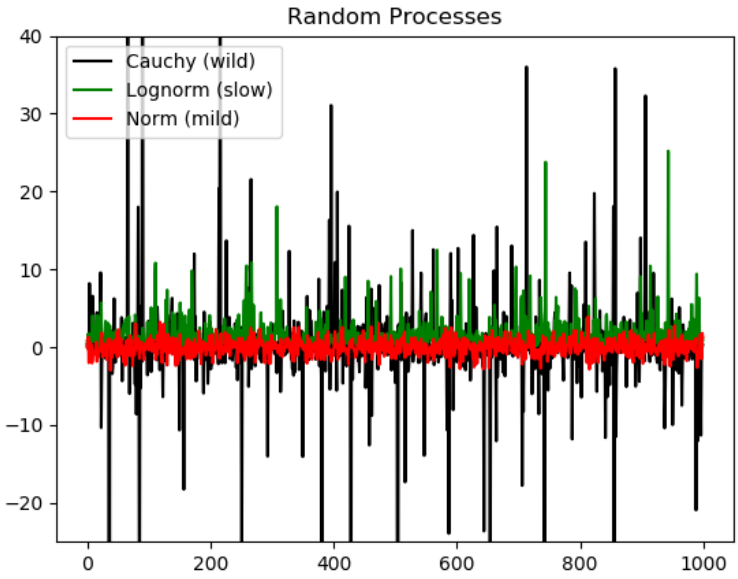

Figure 5.1: Toy model of intermittent behavior with 3 time series. The Gaussian distribution is not intermittent, and leads to no "spikes", but the Cauchy and Lognorm distributions do.

help improve theoretical predictions, it is important to more accurately describe experimental measurements of intermittent fast ion transport.

5.2 Experimental Measurements

Data in this chapter comes from a set of experiments run on DIII-D in oval, inner-wall-limited, L-mode plasmas. These plasmas were run at an electron density of 3×10^{19} m^{-3} and plasma current of 0.8 MA. In all experiments, injected neutral beam power was scanned from 2 MW to 9 MW to alter the source of fast ions as well as the AE amplitude. In several discharges, electron cyclotron heating (ECH) was used near the raidal location of q_{min} to alter the q-profile and stabilize AEs. Measurements were taken from the end of the current ramp phase, as the q-profile settled. In all shots, TAEs were the primary modes driven unstable, and most discharges also had reverse shear AEs (RSAEs) as well.

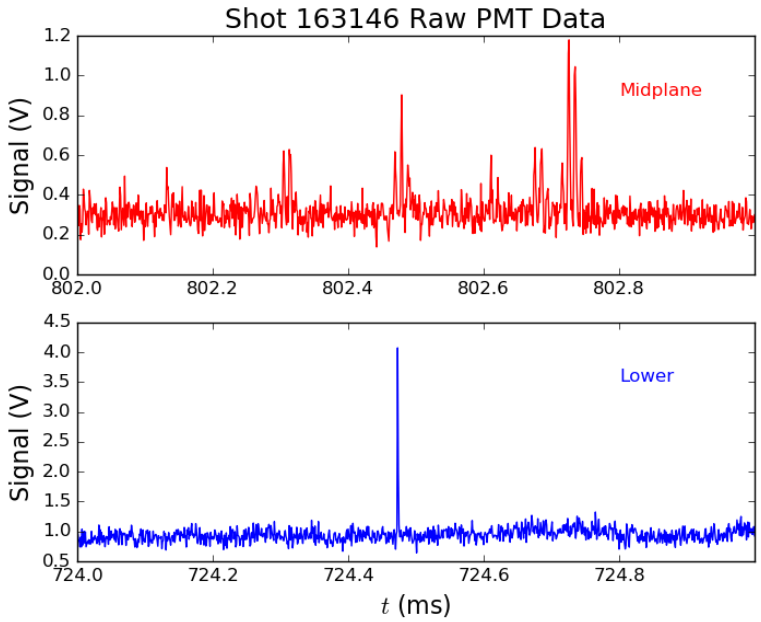

Figure 5.2: FILD data from both probes during a medium power shot without ECH. In the midplane probe (a), short bursts of TAE-induced losses occur, while ithe lower probe (b) saw only individual avalanches.

Data from experiments in 2016 show strong coherent losses from the TAEs in the midplane FILD [6], while the lower probe [15] saw no coherent losses (See Figs 5.2 and 5.3). Instead, the lower probe saw single avalanche-like bursts of signal, which increased in strength and number when beam power was raised. While signal in the midplane FILD was correlated with TAE frequencies, the losses usually come in short bursts of 5 to 10 periods of the TAE, suggesting a secondary mechanism is responsible for sourcing the ions that the TAE pushes into the FILD probes. The inclusion of ECH near q_{min} had a stabilizing effect on RSAEs. Shots with ECH had significantly fewer losses; both coherent losses and avalanches were reduced in number.

Coherent losses can be seen in FILD spectrograms (See Fig 5.3) with the TAE frequencies of ≈ 100 kHz being clearly seen along with a set of both higher and lower frequencies. The higher frequencies appear to correspond to harmonics of the TAE frequencies; however, the lower frequencies appear to be difference frequencies. The high amplitudes at low frequencies

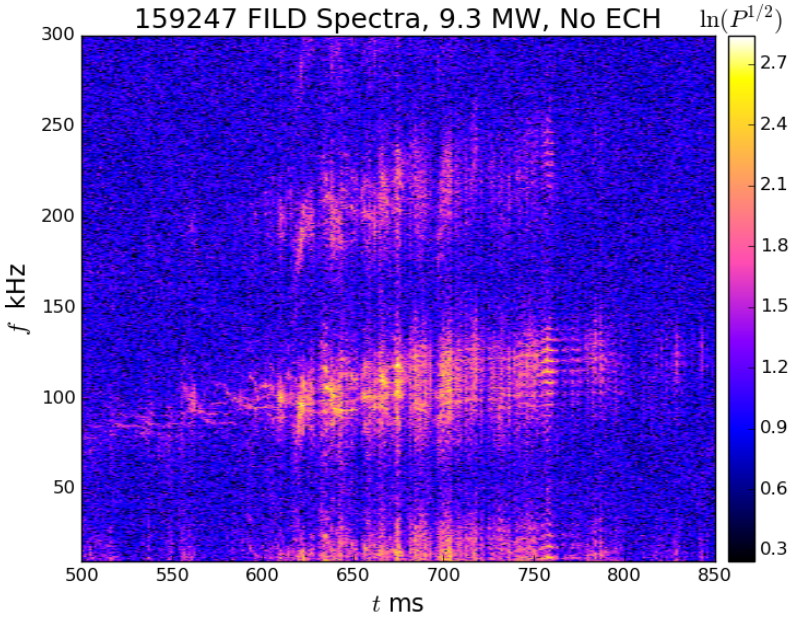

Figure 5.3: Spectrogram of midplane FILD data from a high power shot.

may be related to the temporal spacing between TAE bursts in the midplane FILD data.

Data from 2022 experiments used different neutral beam geometry to source ions and ended up with slightly different results. Both the midplane and lower FILD probes saw coherent losses, with the lower probe detecting more ions later in the discharge. Data from the 2022 campaign did not include strong measurements of EP avalanches when coherent losses were not detected. This may be in part due to the decrease in RSAE activity during these discharges. During this shot, good camera data was available to determine what area of phase space losses were coming from. Losses hitting the midplane probe were full-energy ions in deeply trapped orbits. The lower probe saw two seperate sets of losses (See Fig 5.4): early losses were half-energy ions that were barely trapped, but losses late in the current ramp were full-energy ions on deeply trapped orbits. Tracking these orbits back into the plasma shows that they pass through the outer TAEs on the inner leg of their banana orbits, confirming where they pick up those frequencies.

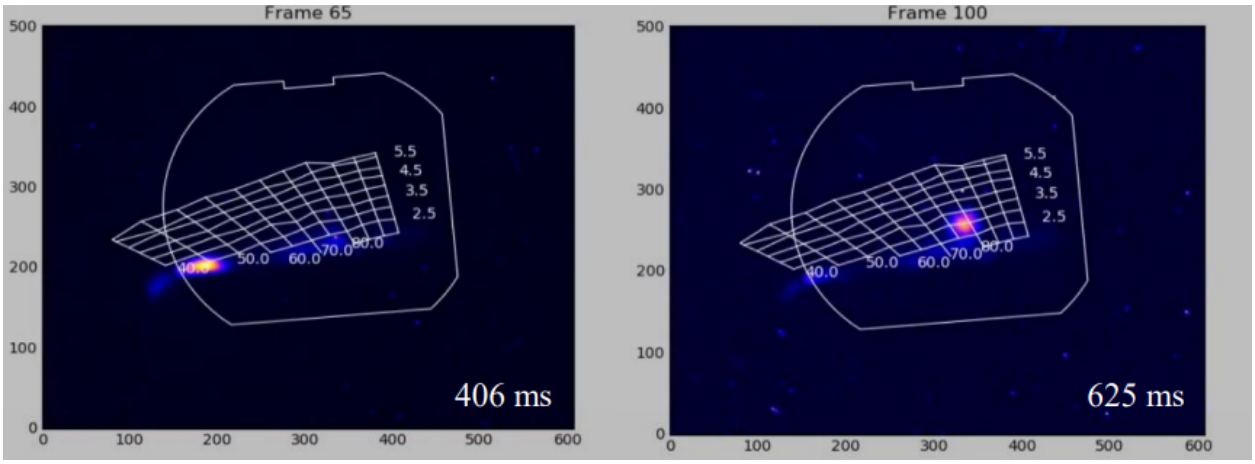

Figure 5.4: Camera data from the lower probe during the 2022 campaign. Early in the shot, losses associated with barely trapped half-energy orbits were measured. Late in the current ramp, full-energy orbits that were deeply trapped hit the detector.

5.3 Quantitative Analysis of FILD Data

Calculation of a Hurst parameter [48, 39] is usually done for a time series that is considered to be in a static position near marginal stability; however, the current ramp of a discharge is a time when the plasma rotation profile is still changing. While this makes use of the calculation harder to use quantitatively, it can still give useful knowledge about the intermittent behavior of the plasma. The Hurst parameter is confined between 0 and 1, and larger values correspond to higher levels of intermittency. Data from the midplane probe in the 2016 campaign shows a clear upward trend in calculation of the Hurst parameter with respect to NBI power (See Fig 5.5). Low power shots have Hurst parameter values near 0.55, while the shots with over 7 MW of injected power have $H \approx 0.8$.

This same trend can be found in both the skewness and kurtosis of the midplane probe data as well. The skewness and kurtosis are the normalized third and fourth moments of the distribution, respectively. For simplicity, we use the Fisher kurtosis, which compares directly to the kurtosis value of a Gaussian distribution. The skewness of the experimental discharges covers an order of magnitude, with the low power shots having a skewness of 0.2

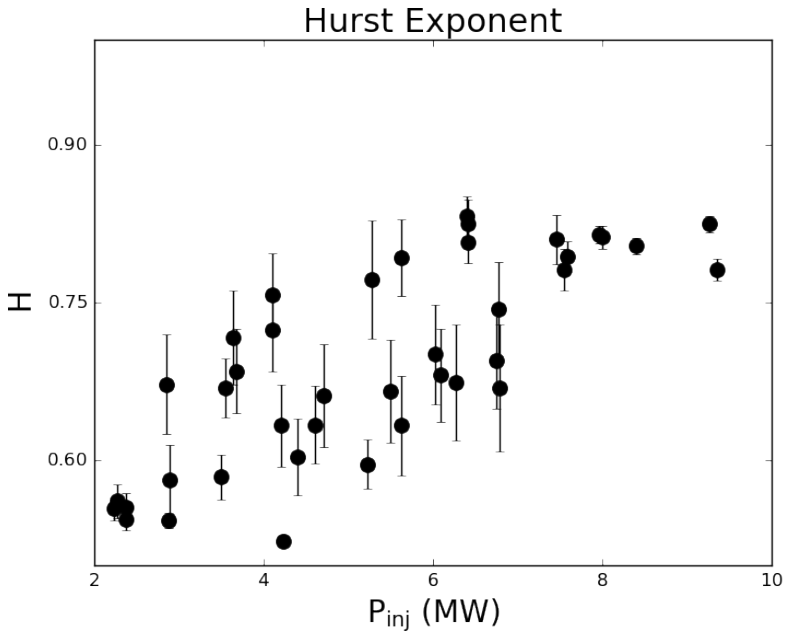

Figure 5.5: Hurst parameter for discharges from 2016 without ECH. A trend of higher intermittency is seen for high beam power.

and the highest power shots reach a skewness of 2.0. The kurtosis covers even more orders of magnitude, from 2.0×10^{-2} at lowest powers to nearly 20 at 6 MW (See Fig 5.6).

The inclusion of ECH breaks the trend of increasing intermittency with beam power. As shown in Fig 5.6, the shots with ECH showed no significant increase in high order moments. This is still useful, however, as it gives a baseline for what the high order moments are without intermittent behavior in the FILD data. Since the kurtosis and skewness of the shots without ECH are the same as those that used ECH below 3 MW of NBI power, we can say that the threshold for the critical gradient must be approxiamtely 3 MW. This is in agreement with the calculations of the Hurst parameter, where the discharges with 2–3 MW of power have similar values.

Shots from the 2022 campaign are not as simple to analyze. The base FILD signal levels rise and fall with the neutron production rate due to self scintillation of the fiber optics used. This means that a single number for skewness and kurtosis is not as good of a fit to a longer

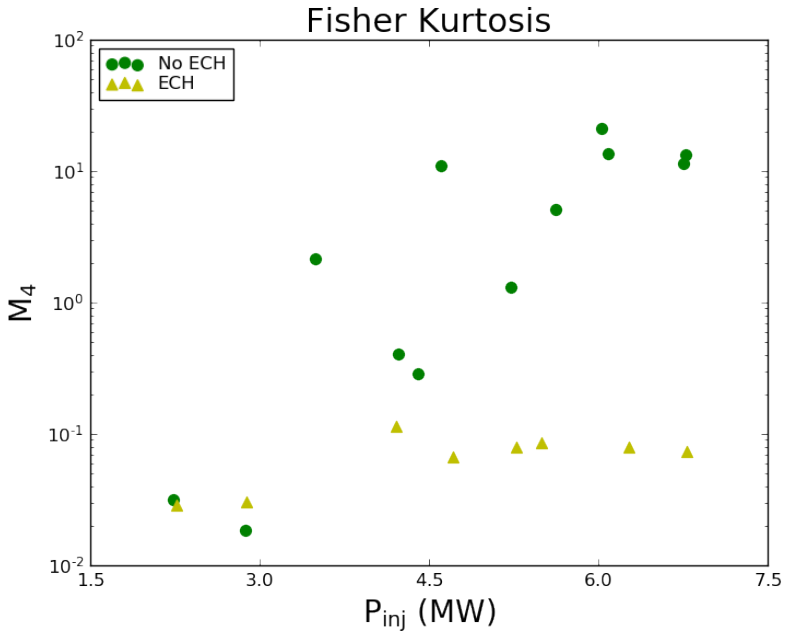

Figure 5.6: Calculated Fisher kurtosis for midplane FILD data from the 2016 campaign. Shots without ECH are in green, and shots using ECH to suppress AEs are in yellow.

time series. Instead, we take a "running" moment by looking at 1 ms time sections of the discharge and computing the skewness and kurtosis over those sections (See Fig 5.7). Values for the higher order moments peak when avalanches occur, with the strongest happening when avalanches saturate the FILD PMTs for a time slice. Values still rise above the background moment levels when coherent losses are strong, but fade away once the probes are no longer being hit.

While no attempt at getting a single value of the Hurst parameter or high order moment showed promise for the midplane probe, the lower probe had some success with finding that the early losses showed an increase in average skewness with higher beam power. What was clear for both probes was that the intensity of avalanche-like events increased with beam power. Unlike the previous campaign, however, the avalanches almost only occurred when coherent losses were also observed.

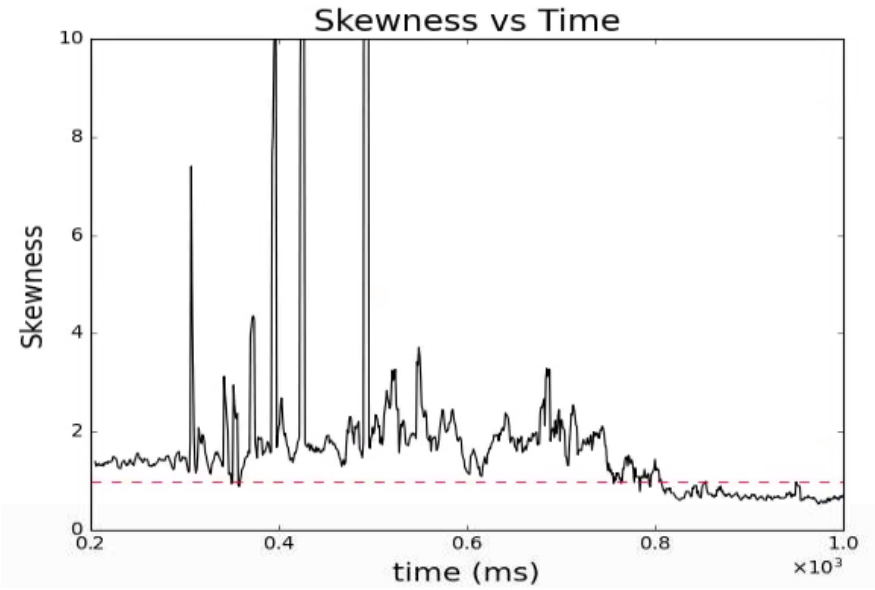

Figure 5.7: Running measure of skewness over 1 ms intervals for midplane FILD data. In the dashed line, the average background skewness level is shown.

5.3.1 Signal Contamination

FILD signals in the recent campaign were contaminated with several signals: background light from neutron signals, increased randomness, and small "spikes" in data from stray radiation. The neutron signal casues a slow change in the background signal, allowing for the calculation of high order moments over shorter periods of time, but the other two signals cause an increase in the calculated moments themselves. In order to determine how which spikes in the data were from background radiation and internal non-Gaussian noise, we analyzed FILD data from several discharges when the toroidal magnetic field was reversed: a magnetic configuration in which the FILDs cannot collect ions.

Spikes in the data were organized by their height and whether or not they lasted for longer than a single time slice. A histogram of spikes for the three PMTs looked at for the 2022 experiment in this work are shown in Fig 5.8. The most important feature of this histogram is the small bump in the height of spikes near 0.15 V for the lower probe and 0.25 V for the midplane FILD. This separation in spike sizes corresponds to the source of the signals;

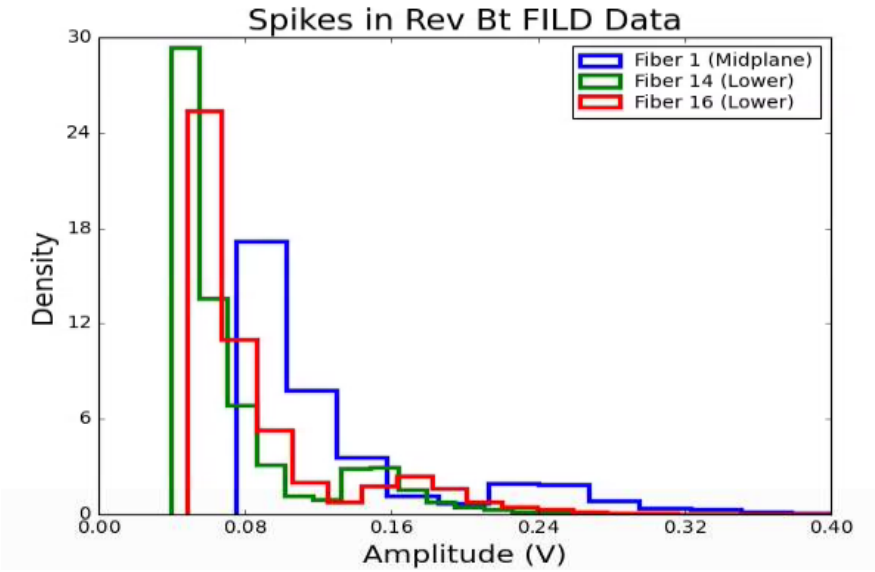

Figure 5.8: Histogram of "spikes" in FILD data during reverse B_t discharges when FILD is unable to collect ions. The smaller spikes are from random non-Gaussian noise, and the bump in slightly larger spikes corresponds to radiation entering the FILD PMT system.

Fiber	Skewness	Kurtosis
FILD01	1.1	1.5
FILD14	1.0	1.2
FILD16	1.1	1.4

Table 5.1: Background skewness and kurtosis levels due to signal contamination in the 2022 campaign as calculated with reverse B_t discharges.

the smaller spikes are simply the largest from non-Gaussian noise, and the larger spikes are from stray radiation contaminating the FILD signals. This also sets a simple minimum size level for analyzing real data — spikes that are smaller than 0.3 V are unlikely to be real avalanches. At the same time, measurement of higher order moments gives the background levels shown in Tab 5.1.

The spikes seen in the reverse B_t shots are also mostly single time-slice bursts, with any extended spikes likely only due to random chance of having both radiation and noise affect the signal at the same times. This is in stark contrast to real data from experiments where we can get ions inside the probes. Real avalanches almost entirely last longer than a single μs timeslice. This suggests that while avalanches may be short lived, they do take an extended

amount of time to finish.

5.4 Conclusion

Characterization of intermittent FILD data shows that there is significant critical gradient behavior in EP losses. Increases in beam power led to more intermittent signals for coherent losses and avalanches as long as ECH was not present. ECH instead cause the RSAEs and intermittency to disappear completely. In the 2022 campaign, RSAE activity was reduced, but still present, and the appearance of intermittent losses remained. The existence of multiple types of AEs that overlap in radial location gives some weight to the theory that overlapping resonances can lead to intermittent transport [55], especially since the disappearance of RSAEs corresponded with the disappearance of both coherent TAE losses in the midplane and avalanches in the lower probe. While the lack of coherent losses with the avalanches still allows for the possibility of particles interacting with two waves to reach a section of phase space that is usually unpopulated by the neutral beams, it is not consistent with a single AE having its damping rate fluctuating with turbulence [59]. This theory may, however, be able to reproduce the short bursts of coherent TAE losses.

FILD data from the 2016 and 2022 campaigns show fairly different results, suggesting the mechanisms behind the losses vary significantly in phase space. Avalanches were observed during coherent TAE losses in the recent experiment, suggesting that both theories of turbulence and resonance overlap may play a role here. Unfortunately, a better understanding of the fast ion transport requires measurements of the confined population to see propagation of avalanches or movement of particles into loss regions. This endeavor will require high speed measurements of the fast ion population via the upgrades to the INPA discussed in Ch 4 as well as turbulence measurements from diagnostics such as Beam Emission Spectroscopy (BES).

Chapter 6

Discussion

Energetic particle transport is a significant area of research towards the efficiency of future fusion reactors. While the details of fast ion movement across the plasma radius can be complicated, the recently upgraded Fast Ion Loss Detectors and Imaging Neutral Particle Analyzer on DIII-D have allowed for progress on understanding transport and loss of EPs for a range of perturbations. At lower frequencies, use of the Light Ion Beam Probe technique determined that the radial kick of fast ion orbits in the presence of externally applied magnetic fields are significant over a wide range of plasma response strengths. At moderate frequencies, the INPA was able to measure signal modulated by an NTM that suggests the LIBP technique can be used for confined particles as well. At higher frequencies, FILD data shows clear intermittent signals in the presence of strong overlapping AE activity.

While this thesis represents novel research in these areas, more work is required to prepare for the prospect of fusion energy. In terms of RMP driven transport, this work concentrated on using the phase difference between two coil sets as a way to change how the plasma responded to the applied magnetic fields; however, this would not suffice for devices that use more than 2 sets of coils for applied RMP control, like ITER. More generalized methods of

determining the poloidal spectra of the RMP fields is necessary for these cases.

Chapter 3 also only looked at lost ions in the RMP fields. While the strength of the vacuum and plasma response fields was strongest near the edge of the plasma, the plasma core still saw some of the perturbation. Simulation and experiment using diagnostics like the INPA would be able to better determine if these fields are capable of causing radial transport of confined ions. While alpha particles in future devices are expected to have large gyroradii that may be less sensitive to smaller perturbations, the fields may become relevant as the helium slows down, possibly even helping get rid of helium "ash".

Future work on the INPA fluctuation measurements of the NTM would allow for full calculations of the expected kick to fast ions in simulations. While Ch 4 makes the claim that the signal seen in experiment is from individual kicks based on the expected small contribution of other sources, a direct comparison would be more complete. This would also help confirm the claim made in this thesis that the two frequencies measured are sourced by different island chains.

The inclusion of the fluctuation measurements in the passing INPA can also see future use in a wide range of experiments unrelated to the NTM shown in this work. Modifications of the optical setup have already begun, and measurements that seem to show AE signals have already been made. We expect this upgrade to be a great improvement to the suite of EP diagnostics on DIII-D in the coming years, and we intend to extend this improvement to the trapped INPA as well.

The work presented in Ch 5 is ongoing, as the theories and simulations that run into intermittent fast ion transport are often concerned with what is happening inside the plasma, and not just at the wall. The fast ion loss data presented is still important, especially at determining how critical gradient behavior can lead not only to stiff EP profiles, but to losses of particles to the wall in bursts; however, measurements from complementary diagnostics

are required to bring this to a satisfying result. The new upgrades to the INPA suggest that with the ability to detect AEs, the INPA may be able to acquire useful data on the confined population for future intermittency experiments. More importantly, if the INPA fluctuations are able to detect avalanches of particles as they move radially through the plasma, this will give us novel data to compare with theory. The BES diagnostic, which measures turbulence across the plasma radius, would also be vital to future experiments. The previous experiment took place while the BES system had suffered damage, but getting good turbulence data to compare with theory is the other component required to see this line of experiment through to the end.

Bibliography

[1] V. V. Afrosimov, I. P. Gladkovskii, Y. S. Gordeev, I. F. Kalinkevich, and N. V. Fedorenko. A method for investigation of the flow of atoms emitted from a plasma. *Zhur. Tekh. Fiz.*, 30, 1960.

[2] M. E. Austin and J. Lohr. Electron cyclotron emission radiometer upgrade on the DIII-D tokamak. *Review of Scientific Instruments*, 74(3):1457–1459, 2003.

[3] D. Carralero, I. Calvo, M. Shoji, B. A. Carreras, K. Ida, S. Ohdachi, S. Sakakibara, H. Yamada, and C. Hidalgo. Influence of β on the self-similarity properties of lhd edge fluctuations. *Plasma Physics and Controlled Fusion*, 53(9):095010, 2011.

[4] B. A. Carreras, B. P. van Milligen, M. A. Pedrosa, R. Balbin, C. Hidalgo, D. E. Newman, E. Sanchez, M. Frances, I. Garcia-Cortes, J. Bleuel, M. Endler, C. Riccardi, S. Davies, G. F. Matthews, E. Martines, V. Antoni, A. Latten, and T. Klinger. Self-similarity of the plasma edge fluctuations. *Physics of Plasmas*, 5(10):3632–3643, 1998.

[5] B. A. Carreras, B. P. van Milligen, M. A. Pedrosa, R. Balbıin, C. Hidalgo, D. E. Newman, E. Sanchez, R. Bravenec, G. McKee, I. Garcia-Cortes, J. Bleuel, M. Endler, C. Riccardi, S. Davies, G. F. Matthews, E. Martines, and V. Antoni. Experimental evidence of long-range correlations and self-similarity in plasma fluctuations. *Physics of Plasmas*, 6(5):1885–1892, 1999.

[6] X. Chen, R. K. Fisher, D. C. Pace, M. García-Muñoz, J. A. Chavez, W. W. Heidbrink, and M. A. Van Zeeland. Near midplane scintillator-based fast ion loss detector on diii-d. *Review of Scientific Instruments*, 83(10):10D707, 2012.

[7] X. Chen, W. Heidbrink, G. Kramer, M. Van Zeeland, M. Austin, R. Fisher, R. Nazikian, D. Pace, and C. Petty. Prompt non-resonant neutral beam-ion loss induced by alfvén eigenmodes in the DIII-d tokamak. *Nuclear Fusion*, 53(12):123019, 2013.

[8] X. Chen, W. W. Heidbrink, M. A. Van Zeeland, G. J. Kramer, D. C. Pace, C. C. Petty, M. E. Austin, R. K. Fisher, J. M. Hanson, R. Nazikian, and L. Zeng. Using neutral beams as a light ion beam probe (invited). *Review of Scientific Instruments*, 85(11):11E701, 2014.

[9] X. Chen, G. Kramer, W. Heidbrink, R. Fisher, D. Pace, C. Petty, M. Podesta, and M. V. Zeeland. Non-linear wave-particle interactions and fast ion loss induced by multiple alfvén eigenmodes in the diii-d tokamak. *Nuclear Fusion*, 54(8):083005, 2014.

[10] C. Collins, W. Heidbrink, M. Podestà, R. White, G. Kramer, D. Pace, C. Petty, L. Stagner, M. Van Zeeland, and Y. ZhuS. Phase-space dependent critical gradient behavior of fast-ion transport due to Alfvén eigenmodes. *Nuclear Fusion*, 57(8):086005, 2017.

[11] C. S. Collins, W. W. Heidbrink, M. E. Austin, G. J. Kramer, D. C. Pace, C. C. Petty, L. Stagner, M. A. Van Zeeland, R. B. White, and Y. B. Zhu. Observation of critical-gradient behavior in alfvén-eigenmode-induced fast-ion transport. *Phys. Rev. Lett.*, 116:095001, 2016.

[12] X. Du, M. Van Zeeland, W. Heidbrink, and D. Su. Development and verification of a novel scintillator-based, imaging neutral particle analyzer in diii-d tokamak. *Nuclear Fusion*, 58(8):082006, 2018.

[13] T. E. Evans. Resonant magnetic perturbations of edge-plasmas in toroidal confinement devices. *Plasma Physics and Controlled Fusion*, 57(12):123001, 2015.

[14] N. M. Ferraro. Calculations of two-fluid linear response to non-axisymmetric fields in tokamaks. *Physics of Plasmas*, 19(5):056105, 2012.

[15] R. K. Fisher, D. C. Pace, M. García-Muñoz, W. W. Heidbrink, C. M. Muscatello, M. A. Van Zeeland, and Y. B. Zhu. Scintillator-based diagnostic for fast ion loss measurements on diii-d. *Review of Scientific Instruments*, 81(10):10D307, 2010.

[16] K. Gage, X. Chen, M. V. Zeeland, W. Heidbrink, J. Hanson, B. Lyons, D. Pace, J. Galdon-Quiroga, and M. Garcia-Munoz. Impact of β_n and spectrum of n = 1 applied fields on fast ion losses in diii-d. *Nuclear Fusion*, 63(3):036002, 2023.

[17] K. Gage, X. Du, W. Heidbrink, J. Gonzalez-Martin, and D. Liu. First fluctuation measurements using an imaging neutral particle analyzer on diii-d. In preparation.

[18] J. Galdon-Quiroga, L. Sanchis-Sanchez, X. Chen, G. Birkenmeier, K. Gage, P. Cano-Megias, J. Gonzalez-Martin, W. Heidbrink, O. Putignano, D. Ryan, G. S. Lopez, B. Tal, M. Van Zeeland, E. Viezzer, M. Willensdorfer, the ASDEX Upgrade Team, and the EUROfusion MST1 Team. Experimental investigation of beam-ion losses induced by magnetic perturbations using the light ion beam probe technique in the asdex upgrade tokamak. *Nuclear Fusion*, 62(9):096004, 2022.

[19] M. García-Muñoz, P. Martin, H.-U. Fahrbach, M. Gobbin, S. Günter, M. Maraschek, L. Marrelli, H. Zohm, and the ASDEX Upgrade Team. Ntm induced fast ion losses in asdex upgrade. *Nuclear Fusion*, 47(7):L10, 2007.

[20] B. Geiger, L. Stagner, W. W. Heidbrink, R. Dux, R. Fischer, Y. Fujiwara, A. Garcia, A. S. Jacobsen, A. J. vanVuuren, A. N. Karpushov, D. Liu, P. A. Schneider, I. Sfiligoi, P. Z. Poloskei, and M. Weiland. Progress in modelling fast-ion d-alpha spectra and neutral particle analyzer fluxes using fidasim. *Plasma Physics and Controlled Fusion*, 2020.

[21] N. Gorelenkov, S. Pinches, and K. Toi. Energetic particle physics in fusion research in preparation for burning plasma experiments. *Nuclear Fusion*, 54(12):125001, 2014.

[22] T. S. Green. A spectrograph for the simultaneous measurement of velocity spectra and charge-to-mass ratios of ions. *Review of Scientific Instruments*, 41(11):1533–1536, 2003.

[23] J. M. Hanson, H. Reimerdes, M. J. Lanctot, Y. In, R. J. L. Haye, G. L. Jackson, G. A. Navratil, M. Okabayashi, P. E. Sieck, and E. J. Strait. Feedback control of the proximity to marginal RWM stability using active MHD spectroscopy. *Nuclear Fusion*, 52(1):013003, 2011.

[24] K. He, Y. Sun, B. Wan, S. Gu, M. Jia, and Y. Hu. Full-orbit simulation of fast ion loss under resonant magnetic perturbations in the EAST tokamak. *Nuclear Fusion*, 61(1):016009, 2020.

[25] J. Heerikhuisen, N. Pogorelov, V. Florinski, G. Zank, and V. Kharchenko. Kinetic modeling of neutral atom transport in the heliosphere. 406:189, 03 2009.

[26] W. W. Heidbrink. Basic physics of alfvén instabilities driven by energetic particles in toroidally confined plasmas. *Physics of Plasmas*, 15(5):055501, 2008.

[27] W. W. Heidbrink, C. S. Collins, M. Podestà, G. J. Kramer, D. C. Pace, C. C. Petty, L. Stagner, M. A. Van Zeeland, R. B. White, and Y. B. Zhu. Fast-ion transport by Alfvén eigenmodes above a critical gradient threshold. *Physics of Plasmas*, 24(5):056109, 2017.

[28] W. W. Heidbrink, Y. Luo, C. M. Muscatello, Y. Zhu, and K. H. Burrell. A new fast-ion Dα diagnostic for DIII-Da). *Review of Scientific Instruments*, 79(10):10E520, 2008.

[29] H. Huang and L. Wang. Effects of resonant magnetic perturbations on the loss of energetic ions in tokamak pedestal. *Plasma Science and Technology*, 22(10):105101, 2020.

[30] J. W. Hughes, N. T. Howard, P. Rodriguez-Fernandez, A. J. Creely, A. Q. Kuang, P. B. Snyder, T. M. Wilks, R. Sweeney, and M. Greenwald. Projections of h-mode access and edge pedestal in the sparc tokamak. *Journal of Plasma Physics*, 86(5):865860504, 2020.

[31] R. K. Janev and J. J. Smith. *Cross sections for collision processes of hydrogen atoms with electrons, protons and multiply charged ions*. Number 4 in Atomic and Plasma–Material Interaction Data for Fusion. International Atomic Energy Agency, Vienna, 1993.

[32] M. Jiménez-Ramos, J. García López, M. García-Muñoz, M. Rodríguez-Ramos, M. Carmona Gázquez, and B. Zurro. Characterization of scintillator materials for fast-ion loss detectors in nuclear fusion reactors. *Nuclear Instruments and Methods in Physics Research Section B: Beam Interactions with Materials and Atoms*, 332:216–219, 2014. 21st International Conference on Ion Beam Analysis.

[33] J. D. King, E. J. Strait, R. L. Boivin, D. Taussig, M. G. Watkins, J. M. Hanson, N. C. Logan, C. Paz-Soldan, D. C. Pace, D. Shiraki, M. J. Lanctot, R. J. La Haye, L. L. Lao, D. J. Battaglia, A. C. Sontag, S. R. Haskey, and J. G. Bak. An upgrade of the magnetic diagnostic system of the diii-d tokamak for non-axisymmetric measurements. *Review of Scientific Instruments*, 85(8):083503, 2014.

[34] S. Li, H. Jiang, Z. Ren, and C. Xu. Optimal tracking for a divergent-type parabolic pde system in current profile control. *Abstract and Applied Analysis*, 2014(1085-3375):940965, 2014.

[35] D. Lin, X. Du, W. Heidbrink, and M. Van Zeeland. Validation of the imaging neutral particle analyzer in nearly mhd quiescent plasmas using injected beam ions on diii-d. *Nuclear Fusion*, 60(11):112008, 2020.

[36] A. Loarte, G. Saibene, R. Sartori, M. Becoulet, L. Horton, T. Eich, A. Herrmann, M. Laux, G. Matthews, S. Jachmich, N. Asakura, A. Chankin, A. Leonard, G. Porter, G. Federici, M. Shimada, M. Sugihara, and G. Janeschitz. Elm energy and particle losses and their extrapolation to burning plasma experiments. *Journal of Nuclear Materials*, 313-316:962–966, 2003. Plasma-Surface Interactions in Controlled Fusion Devices 15.

[37] R. H. Majeed and O. N. Oudah. Reaching to a featured formula to deduce the energy of the heaviest particles producing from the controlled thermonuclear fusion reactions. *Journal of Physics: Conference Series*, 1003(1):012076, 2018.

[38] B. B. Mandelbrot. *Fractals and Scaling in Finance*. Springer New York, New York, NY, 1997.

[39] B. B. Mandelbrot and J. R. Wallis. Noah, Joseph, and operational hydrology. *Water Resources Research*, 4(5):909–918, 1968.

[40] C. M. Muscatello, W. W. Heidbrink, R. L. Boivin, C. Chrystal, C. S. Collins, Y. Fujiwara, and H. Yamaguchi. Diagnosis of fast ions produced by negative-ion neutral-beam injection with fast-ion deuterium-alpha spectroscopy. *Review of Scientific Instruments*, 90(7):073504, 2019.

[41] B. Nouhi, N. Darabi, P. Sareh, H. Bayazidi, F. Darabi, and S. Talatahari. The fusion–fission optimization (fufio) algorithm. *Scientific Reports*, 12:12396, 2022.

[42] K. Ogawa, S. Bozhenkov, S. Äkäslompolo, C. Killer, O. Grulke, D. Nicolai, G. Satheeswaran, M. Isobe, M. Osakabe, M. Yokoyama, and R. Wolf. Energy-and-pitch-angle-resolved escaping beam ion measurements by faraday-cup-based fast-ion loss detector in wendelstein 7-x. *Journal of Instrumentation*, 14(09):C09021, 2019.

[43] A. Pankin, D. McCune, R. Andre, G. Bateman, and A. Kritz. The tokamak monte carlo fast ion module nubeam in the national transport code collaboration library. *Computer Physics Communications*, 159(3):157–184, 2004.

[44] H. Reimerdes, M. S. Chu, A. M. Garofalo, G. L. Jackson, R. J. La Haye, G. A. Navratil, M. Okabayashi, J. T. Scoville, and E. J. Strait. Measurement of the resistive-wall-mode stability in a rotating plasma using active mhd spectroscopy. *Phys. Rev. Lett.*, 93:135002, 2004.

[45] T. Rhodes, R. Moyer, R. Groebner, E. Doyle, R. Lehmer, W. Peebles, and C. Rettig. Experimental evidence for self-organized criticality in tokamak plasma turbulence. *Physics Letters A*, 253(3):181–186, 1999.

[46] J. F. Rivero-Rodriguez, M. Garcia-Munoz, R. Martin, J. Galdon-Quiroga, J. Ayllon-Guerola, R. J. Akers, J. Buchanan, D. Croft, D. Garcia-Vallejo, J. Gonzalez-Martin, D. Harvey, K. G. McClements, M. Rodriguez-Ramos, and L. Sanchis. A rotary and reciprocating scintillator based fast-ion loss detector for the MAST-U tokamak. *Review of Scientific Instruments*, 89(10):10I112, 2018.

[47] J. Rivero-Rodríguez, J. Galdon-Quiroga, J. Domínguez-Palacios, M. García-Muñoz, D. Garcia-Vallejo, J. Gonzalez-Martin, K. McClements, L. Sanchís, K. Särkimäki, A. Snicker, Y. Todo, L. Velarde, E. Viezzer, and the ASDEX Upgrade Team. Transport and acceleration mechanism of fast ions during edge localized modes in asdex upgrade. *Nuclear Fusion*, 63(8):086028, 2023.

[48] R. Sanchez and D. E. Newman. Self-organized criticality and the dynamics of near-marginal turbulent transport in magnetically confined fusion plasmas. *Plasma Physics and Controlled Fusion*, 57(12):123002, 2015.

[49] L. Sanchis, M. Garcia-Munoz, A. Snicker, D. A. Ryan, D. Zarzoso, L. Chen, J. Galdon-Quiroga, M. Nocente, J. F. Rivero-Rodriguez, M. Rodriguez-Ramos, W. Suttrop, M. A. Van Zeeland, E. Viezzer, M. Willensdorfer, and F. Z. and. Characterisation of the fast-ion edge resonant transport layer induced by 3d perturbative fields in the ASDEX upgrade tokamak through full orbit simulations. *Plasma Physics and Controlled Fusion*, 61(1):014038, 2018.

[50] L. Stagner, B. Geiger, and W. Heidbrink. FIDASIM: A Neutral Beam and Fast-ion Diagnostic Modeling Suite.

[51] E. J. Strait. Magnetic diagnostic system of the diii-d tokamak. *Review of Scientific Instruments*, 77(2):023502, 2006.

[52] E. J. Strait. Magnetic diagnostic system of the DIII-D tokamak. *Review of Scientific Instruments*, 77(2):023502, 2006.

[53] Y. Todo. Introduction to the interaction between energetic particles and alfven eigenmodes in toroidal plasmas. *Reviews of Modern Plasma Physics*, 3(1), 2018.

[54] Y. Todo and T. Sato. Linear and nonlinear particle-magnetohydrodynamic simulations of the toroidal Alfvén eigenmode. *Physics of Plasmas*, 5(5):1321–1327, 1998.

[55] Y. Todo, M. V. Zeeland, and W. Heidbrink. Fast ion profile stiffness due to the resonance overlap of multiple alfvén eigenmodes. *Nuclear Fusion*, 56(11):112008, 2016.

[56] M. Van Zeeland, N. Ferraro, B. Grierson, W. Heidbrink, G. Kramer, C. Lasnier, D. Pace, S. Allen, X. Chen, T. Evans, M. García-Muñoz, J. Hanson, M. Lanctot, L. Lao, W. Meyer, R. Moyer, R. Nazikian, D. Orlov, C. Paz-Soldan, and A. Wingen. Fast ion transport during applied 3d magnetic perturbations on DIII-d. *Nuclear Fusion*, 55(7):073028, 2015.

[57] M. A. Van Zeeland, N. M. Ferraro, W. W. Heidbrink, G. J. Kramer, D. C. Pace, X. Chen, T. E. Evans, R. K. Fisher, M. García-Muñoz, J. M. Hanson, M. J. Lanctot, L. L. Lao, R. A. Moyer, R. Nazikian, and D. M. Orlov. Modulation of prompt fast-ion loss by appliedn= 2 fields in the DIII-d tokamak. *Plasma Physics and Controlled Fusion*, 56(1):015009, 2013.

[58] J. Varje, K. Särkimäki, J. Kontula, P. Ollus, T. Kurki-Suonio, A. Snicker, E. Hirvijoki, and S. Äkäslompolo. High-performance orbit-following code ASCOT5 for monte carlo simulations in fusion plasmas, 2019.

[59] R. Waltz, E. Bass, C. Collins, and K. Gage. Quasilinear critical gradient model for alfven eigenmode driven energetic particle transport with intermittency. *Nuclear Fusion*, 61(3):036043, 2021.

[60] W. Wen-Hao, Y. Chang-Xuan, W. Yi-Zhi, X. Yu-Hong, L. Bi-Li, G. Xian-Zu, L. Bao-Hua, and W. Bao-Nian. Self-organized criticality properties of the turbulence-induced particle flux at the plasma edge of the ht-6m tokamak. *Chinese Physics Letters*, 18(6):793, 2001.

[61] R. Wenninger, M. Bernert, T. Eich, E. Fable, G. Federici, A. Kallenbach, A. Loarte, C. Lowry, D. McDonald, R. Neu, T. Pütterich, P. Schneider, B. Sieglin, G. Strohmayer, F. Reimold, and M. Wischmeier. DEMO divertor limitations during and in between ELMs. *Nuclear Fusion*, 54(11):114003, 2014.

[62] Y. B. Zhu, A. Bortolon, W. W. Heidbrink, S. L. Celle, and A. L. Roquemore. Compact solid-state neutral particle analyzer in current modea). *Review of Scientific Instruments*, 83(10):10D304, 2012.

[63] S. J. Zweben, R. L. Boivin, R. E. Duvall, E. D. Fredrickson, R. J. Goldston, H. E. Mynick, J. D. Strachan, and R. B. White. MeV ion confinement in the TFTR tokamak. *Physics of Fluids B: Plasma Physics*, 2(6):1411–1414, 1990.

Appendix A

Diagnostic Data Acquisition

The hardware for the data acquisition systems of the Fast Ion Loss Detectors and Imaging Neutral Particle Analyzers were set up to be nearly identical. Both FILDs and the passing INPA use a beam splitter to include an array of visible wavelength fiber optics to a set of PMTs. Nearly all power supplies are shared between all PMTs. There are 2 supplies for the PMT bias voltages: 1 for the FILDs and the other for the INPA. The camera hardware is equivalent for all FILDs and INPAs on DIII-D (See Fig A.1).

The pco panda camera that is used on the probes requires a USB 3.0 connection to send data to the FILD servers. Since the servers cannot survive in the machine hall environment, and the distance between the probes and computers cannot be linked via USB cables without significant signal degradation, we use a set of Black Box USB 3.0 extenders to connect to the diagnostic via OM3 fibers. Testing has found that these extenders can fail during plasma discharges due to the strong magnetic fields if located close to the midplane of the machine, so they have been moved into suitable locations. Unlike the previous cameras used on DIII-D, the pco pixelfly, the pandas do not accept a pulse train for image capture from the same input that the controlling PC is connected to. In this case, signal from our pulse generator

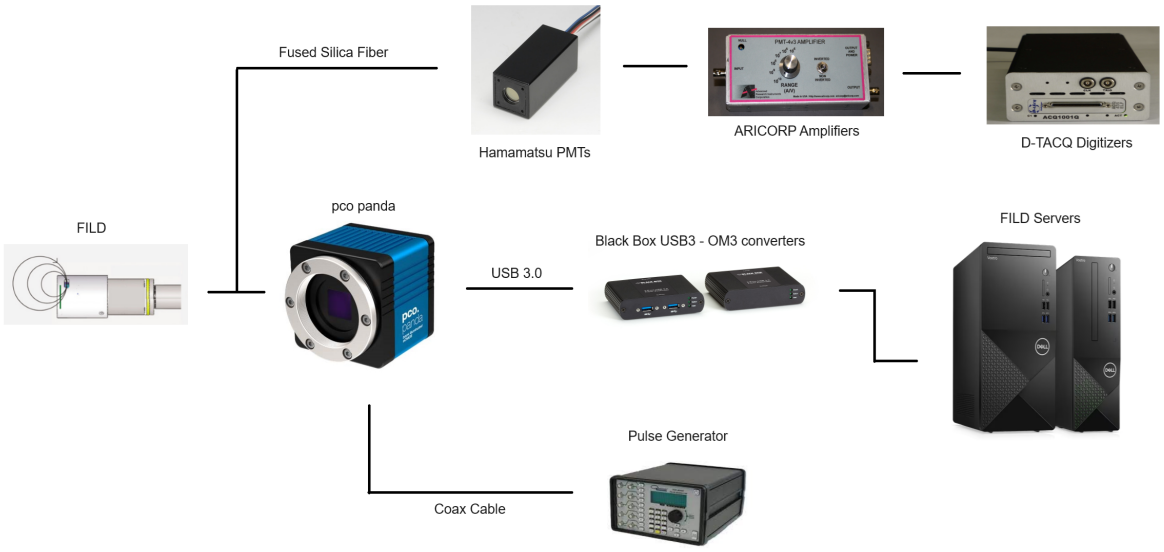

Figure A.1: Schematic of FILD data acquisition systems on DIII-D. The passing INPA has an equivalent setup, while the trapped INPA does not yet include a fluctuation measurement setup.

is routed to the machine hall via coax cables to allow for this mode of setting the frame rate and exposure times.

Several pieces of software are used in the data acquisition and analysis steps for camera data from the FILDs. The first is the prepackaged program CamWare from pco that can operate the cameras. While use of the previous pixelfly cameras used manual operation via the CamWare software, this software is now only used for doing calibration of the diagnostics. The use of the live view included in the software allows for proper alignment of the camera during installation. This is done by illuminating the FILD scintillators with a set of embedded UV LEDs and operating the pco panda in live view mode while attaching it to the camera mount. Once secure, the CamWare program can be used to determine the best Region of Interest (ROI) on the CCD chip to use, and take a single algnment image. This image can then be ran through a simple python script that plots an overlay of the scintillator boundary on top of the image to determine the correct alignment for strike map calculations.

A separate set of python scripts has been set up to operate the cameras during experiments. Some of these scripts are used as wrappers for the C++ code in the pco software development kit that comes with the cameras. The full acquisition process is split into 2 separate flows. The first script prepares the camera settings — including ROI, exposure settings, pixel binning, maximum frames to be recorded, etc. — and then waits for a system event that is triggered 19 seconds prior to the start of a discharge (T-19). After receiving this signal, the current shot is checked to determine if it will be a plasma discharge. If so, the script boots the camera and ensures all settings are correct. The camera then waits until it receives signal from the pulse generator used to set the frame timing. Currently, we have the pulse generator send 2 ms pulses at a rate of 160 Hz. If the camera takes enough frames to hit the programmed limit or waits 20 seconds without being sent a new pulse, the camera stops recording and saves the current data along with relevant metadata. Then the camera is shut down to reduce heat generation and the process waits for the next T-19 event. The second script is used to combine the camera data with the metadata in an HDF5 format file and upload it onto a DIII-D server for future access. The metadata includes the camera settings, calibration alignment settings, and the total number of frames taken.

Once the images have been uploaded to the DIII-D server, they are available to download and analyze. This is most easily done with a set of code called FILDcam (See Fig A.2), a graphical user interface specifically for DIII-D FILD camera data that was rewritten from IDL to python. This code has several features, including the following:

- Download videos from either FILD probe,
- Determine the time during the shot that a frame was taken using the frame rate and start time
- Smooth the data using a simple 2D convolution
- Overplot the scintillator boundary and strike map, if calculated,

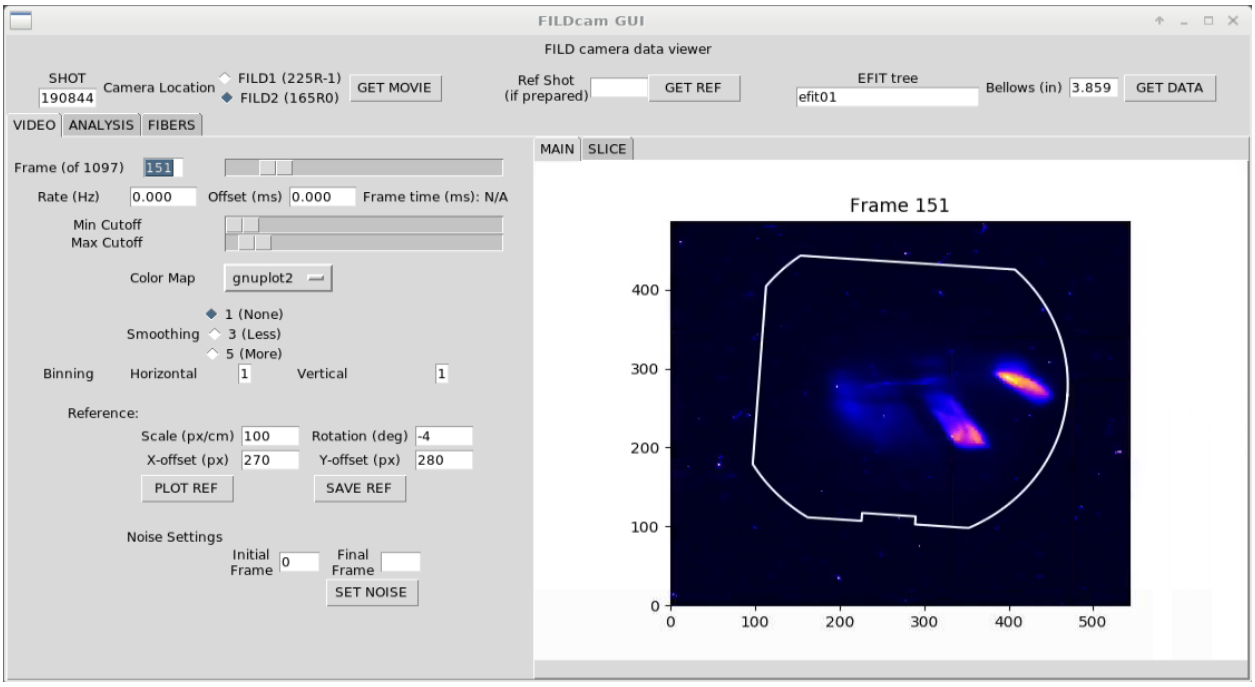

Figure A.2: Example session using the FILDcam GUI. This shows camera data with a scintillator boundary overlay prior to calculation of a strike map.

- Subtract an average background from each frame,
- Plot the signal strength along a vertical or horizontal slice, and
- Calculate strike maps of varying resolution.

These allow for quick analysis of camera data for simple applications. More in-depth analysis that is tailored to specific experimental needs usually must be done manually.